Mechanisms of motor-independent membrane remodeling driven by dynamic microtubules

Ruddi Rodríguez-García[1], Vladimir A. Volkov[2], Chiung-Yi Chen[1], Eugene A. Katrukha[1], Natacha Olieric[3], Amol Aher[1], Ilya Grigoriev[1], Magdalena Preciado López[5], Michel O. Steinmetz[3,4], Lukas C. Kapitein[1], Gijsje Koenderink[5], Marileen Dogterom[2*] and Anna Akhmanova[1*]

[1] Cell Biology, Department of Biology, Faculty of Science, Utrecht University, 3584 CH Utrecht, the Netherlands.

[2] Department of Bionanoscience, Kavli Institute of Nanoscience, Delft University of Technology, 2629HZ Delft, the Netherlands

[3] Laboratory of Biomolecular Research, Department of Biology and Chemistry, Paul Scherrer Institut, 5232 Villigen, Switzerland

[4] University of Basel, Biozentrum, CH-4056 Basel, Switzerland

[5] Department of Living Matter, AMOLF, Science Park 104, 1098 XG Amsterdam, the Netherlands

*Corresponding authors: m.dogterom@tudelft.nl; a.akhmanova @uu.nl

Abstract

Microtubule-dependent organization of membrane organelles, such as the endoplasmic reticulum, occurs through motor-based pulling and by coupling polymer dynamics to membrane remodeling. Membrane binding to dynamic microtubule ends involves transient interactions, but how such interactions can lead to membrane deformation is unclear. Here, we reconstitute membrane tubulation in a minimal system with giant unilamellar vesicles, dynamic microtubules, End-Binding (EB) proteins and a membrane-targeted polypeptide that interacts with EBs and microtubules. We demonstrate that these components are sufficient to induce not only membrane tubulation by growing microtubule ends, but also motor-independent membrane sliding along microtubule shafts and tube pulling by shrinking microtubules. Experiments and modeling reveal that the first two mechanisms can be explained by adhesion-driven biased membrane spreading on microtubules. Attachments to growing and shrinking microtubule ends can sustain forces of ~0.5 and ~5 pN, respectively. Rapidly exchanging molecules that connect membranes to dynamic microtubules can thus induce membrane tubulation and processive tube motility.

Introduction

Membrane-bound cellular organelles can acquire complex shapes, which are essential for their functions. Defects in organelle morphology and distribution can affect cell viability and lead to human diseases[1-3]. Formation of membrane structures with high curvature, such as tubules, is energetically unfavorable and thus requires applied forces[4-8]. In cells, the generation and stabilization of curved membranes depends on membrane-deforming proteins and the cytoskeleton[6-9].

Microtubules (MTs) are major cytoskeletal filaments, and the forces generated by MTs are important for many cellular processes[10, 11]. Dynamic MTs generate pushing and pulling forces with the magnitude of several pN[12, 13]. Pushing forces are observed when a MT polymerizes against an obstacle such as a membrane; these forces can be used to position intracellular structures as well as whole MT networks like the mitotic spindle[10, 14]. Pulling forces in turn are generated through protein attachment to depolymerizing MTs; these forces play a crucial role in chromosome separation during cell division but can also have other functions[15-17]. Finally, MT-based molecular motors, kinesins and dyneins, can generate force to position and shape cellular organelles[18].

The endoplasmic reticulum (ER) is a complex membrane structure, which adopts a variety of morphologies ranging from the nuclear envelope to dynamic tubules. These morphologies depend on specific membrane-shaping proteins[19] and on the interactions with the cytoskeleton[3]. In particular, several types of MT-based processes have been implicated in the extension and positioning of ER tubules. First, ER tubules can extend along pre-existing MTs in a process termed sliding, which can be driven by MT-based molecular motors[20-23]. Second, an ER tubule can be formed when a membrane attaches to the plus end of a growing MT via a membrane-MT tip attachment complex (TAC)[16, 20, 21, 24].

Third, recent work has shown that ER tubules can be pulled by depolymerizing MT ends (a mechanism termed dTAC, the molecular basis of which is currently unknown)[24].

Experiments in cells demonstrated that TAC formation requires two types of MT plus-end tracking proteins (+TIPs): End Binding (EB) proteins, which recognize the stabilizing cap at growing MT ends[25], and the ER-resident transmembrane protein STIM1[21]. STIM1 specifically accumulates at the plus ends of growing MTs in an EB-dependent manner, because it contains a linear SxIP motif that binds to the C-terminal part of EB proteins [26].

The extraction of membrane tubes by MT motors that move on stabilized microtubules has been extensively studied by *in vitro* reconstitution experiments[27-31]. In contrast, membrane re-shaping through coupling to dynamic MTs is poorly understood. For example, it is unclear whether the two known TAC components, an EB protein and a membrane associated EB partner, are sufficient for membrane tube formation by a growing MT. It is also unclear how +TIPs, which arrive to growing MT tips by diffusion and rapidly exchange at these ends[32, 33], can mediate forces that induce membrane tubulation and promote processive tube motility. Finally, it is currently unknown whether dTACs can be driven by the same molecules that are responsible for TAC formation.

Here, we show that membrane tubulation by sliding, TAC and dTAC mechanisms can be reconstituted in a minimal *in vitro* system containing dynamic MTs, an EB protein and a membrane-bound polypeptide that could interact with MTs and EBs. The magnitude of the force generated by TAC- and dTAC-mediated mechanisms is in the range of 0.5 pN and 5 pN, respectively. Motor-independent membrane sliding and TAC-based membrane remodeling can be explained by adhesion-driven spreading of membranes on MTs. The combination of experiments and modeling described here thus reveals how dynamic MTs combined with non-motor proteins that link MTs and membranes generate force for membrane remodeling.

Results

A membrane-bound SxIP motif-containing protein and EB3 promote membrane tube extension by dynamic MTs

To investigate the mechanism of force generation underlying TAC-based membrane extension, we reconstituted the interaction between membranes and MTs in a system with a minimal set of components (Fig. 1a). We used giant unilamellar vesicles (GUVs) prepared from POPC (94.95%), DOGS-NTA-Ni (5%) and Rh-PE (0.05%) (Fig.1a,b). MTs were grown from GMPCPP-stabilized MT seeds as described previously[32, 34] in the presence of tubulin, mCherry-EB3 and an SxIP motif-containing polypeptide (termed His-GFP-SxIP), which was derived from the C-terminus of human MACF2 and which we have extensively characterized previously[26]. This polypeptide was dimerized using the leucine zipper from GCN4 and tagged with the green fluorescent protein (GFP) and a 6-Histidine tag (His), which could bind to the Ni-NTA moiety on the GUV surface (Fig. 1a,b). MTs and GUVs were visualized using Total Internal Reflection Fluorescence (TIRF) or confocal microscopy.

In the assay with dynamic MTs, His-GFP-SxIP was strongly enriched at growing MT ends in an EB3-dependent manner, consistent with previous reports[26], and its accumulation at MT tips increased at higher EB3 concentrations (Fig. 1c, Supplementary Fig. S1a-d). Furthermore, His-GFP-SxIP was weakly bound along MT shafts (Fig.1c), likely because MTs are negatively charged and the polypeptide is positively charged; this binding was EB3-independent. When GUVs were included in the assay, His-GFP-SxIP was recruited to the GUV surface, and the concentration of free His-GFP-SxIP in solution decreased over time (Fig. 1b, Supplementary Fig. S1c). His-GFP-SxIP can thus potentially mediate the interaction between GUVs and MTs.

When GUVs were combined with MTs, within a few minutes, membrane tubes started to form (Fig. 1d). These tubes co-localized with MTs, which were visualized using SiR-tubulin, a fluorescent probe based on the silicon-rhodamine and the MT-binding drug Docetaxel (Fig. 1e), indicating that MTs supported membrane tube extension. Earlier studies reported generation of tubular networks when GUVs were incubated with stable MTs and motors[28-31, 35]. In contrast, our assay did not include motor proteins, demonstrating that a motor-independent MT-based mechanism can extract tubes from a lipid vesicle.

We next investigated the effect of EB3 and His-GFP-SxIP on membrane tube formation. To characterize membrane morphology, we measured the GUV sphericity and the total length of all tubes in the network formed by each liposome[29, 36](Fig. 2a-c and Supplementary Fig. S1e). In the absence of His-GFP-SxIP, GUVs preserved their round shape even at a high (200 nM) EB3 concentration, and the transition to the tubular regime did not occur (Fig. 2a-d). In contrast, in the presence of His-GFP-SxIP and in the absence of EB3, some tubes were observed and the number of detected tubes increased with the His-GFP-SxIP concentration (Fig. 2a,c,d). Short tubes could be detected at 200 nM EB3 and 5 nM His-GFP-SxIP (Fig. 2a,c,d); however, only when the concentration of His-GFP-SxIP was increased to 15 nM in the presence of 200 nM EB3, extensive tubulation of 90% of the GUVs was observed (Fig. 2a-d). These data indicate that MT-driven membrane tubulation can be reconstituted using proteins that couple membranes to dynamic MTs.

To test whether MT-membrane interaction can be supported by EB3 alone, we used its 6-Histidine-tagged version (His-EB3) that could directly interact with growing MT tips and DOGS-NTA-Ni on the GUV surface. However, even at 200 nM His-EB3, only short tubular structures were present on 50% of the GUVs (Fig. 2d-f), likely because the affinity of EB3 for MT shafts is low. These results indicate that an EB3 protein directly

linked to membranes can promote some membrane tubulation, but the generation of long membrane tubes occurs much more efficiently when an EB3 protein is combined with a MT-binding membrane-attached peptide.

MT-dependent membrane tubulation is limited by tension

Previous studies have shown that ligand-dependent adhesion of GUVs to the surface of a solid substrate or to a nanofiber triggered the formation of membrane tubules[37-39]. When a GUV faces an adhesive substrate in the presence of mobile ligands, the ligands that bind to the substrate move to the contact region and increase the adhesion strength[40, 41]. We investigated whether His-GFP-SxIP was enriched in the regions where GUVs interacted with MTs and found that the average fluorescence intensity of the His-GFP-SxIP on MTs bound to the membrane was indeed higher than on free MTs or membranes that were not in contact with MTs (Fig. 3a,b). His-GFP-SxIP proteins thus converged towards the sites of MT-membrane contact, suggesting an increase in the number of bonds between the two structures.

Next, we investigated the dynamics of formation of tubular membrane networks by measuring GUV sphericity[36] over time. At the beginning of the assay, sphericity quickly decreased, indicating that the network of membrane tubes rapidly expanded (Fig. 3c,d). At later time points, the sphericity value became almost constant as tube extension slowed down (Fig. 3c,d, and Supplementary Video 1). We hypothesized that this was caused by the increase in lateral tension after the excess of membrane area was used up due to membrane redistribution into tubes[42-45]. To test this possibility, we characterized thermal membrane fluctuations, which are controlled by the balance between thermal energy, lateral tension and membrane stiffness[4, 5]. Flickering spectroscopy[46, 47] was used to analyze membrane undulations in freely fluctuating GUVs and GUVs attached to MTs (Fig.

3e). Fluctuations of the vesicle radius were recorded at the equatorial plane by video microscopy (Fig. 3e,f) and expanded in series of discrete Fourier modes n=2,3…50. We then calculated the time-average of quadratic fluctuation amplitudes. The experimentally estimated amplitudes were corrected for the noise caused by the finite spatial resolution of the imaging (pixelization) and plotted as a function of the mode n, known as a fluctuation spectrum (FS)(Fig. 3g, Supplementary Fig. S1f). In the presence of MTs, the amplitude of membrane fluctuations was reduced by an order of magnitude (Fig. 3g), with amplitudes lower than our detection limit at high fluctuation modes. The elastic modulus that we measured (Fig. 3h) was in good agreement with previously published values[47], indicating the similarity in membrane stiffness in both conditions. Importantly, lateral membrane tension was significantly higher in the presence of MTs, leading to the reduction in the amplitude of fluctuations (Fig. 3g,h). Taken together, our data indicate that GUV extension along MTs follows previously described membrane adhesion dynamics[44, 48-50], where the initial spreading is counteracted by lateral membrane tension.

Membrane remodeling occurs by three mechanisms

To understand better how membrane tubes are pulled in our assay, we investigated their dynamics in more detail. We observed some membrane tubes sliding along MT shafts (Fig. 4a, Supplementary Fig. S2a and Supplementary Video 2). Sliding tubes typically moved faster than the elongation rate of a growing MT end (Fig. 4b,d). When the tip of a sliding membrane tube reached the end of a growing MT, the membrane slowed down because it could not extend beyond the MT tip and its spreading was thus limited by the speed of MT growth (Fig. 4b,c and Supplementary Video 3). A growing MT end could also initiate tube formation without prior spreading along a pre-existing MT (Supplementary Fig. S2b). Interestingly, the interaction of a membrane with a MT end slowed down the rate of

MT growth (Fig. 4d). One potential reason for this effect is the decrease in tubulin diffusion to the MT tip caused by membrane shielding. This conclusion is supported by the observation that a similar effect was observed also in the absence of His-GFP-SxIP (Fig. 4d), in conditions where there was no direct interaction between the MT and the membrane.

Recent work using structured illumination microscopy in living cells demonstrated that ER tubules could be pulled by depolymerizing MT ends (dTAC)[24]. Such events were also observed in our assays, where shrinking MTs could extract long membrane tubes from GUVs (Fig. 4e, Supplementary Fig. S2c and Supplementary Video 4). At the tips of dTAC-driven membrane tubes, we observed an accumulation of His-GFP-SxIP, but not of EB3 (Fig. 4e, Supplementary Fig. S2c and Supplementary Video 4). Strikingly, the shortening rate of MTs that were in contact with a membrane was reduced ~ 3 fold (Fig. 4f). Shortening MT ends have a distinct structure compared to the growing ones, with tubulin protofilaments being more bent. Protein complexes capable of following shrinking MT ends were shown to be able to slow down the speed of MT disassembly[51-53]. It is thought that proteins interacting with bent tubulin protofilaments, which exert a power stroke during MT disassembly, can transmit force from a depolymerizing MT end to a cargo, causing its displacement[54, 55]. Our results suggest that membrane-bound His-GFP-SxIP proteins accumulating at the interface between the depolymerizing MT and the membrane create an attachment site that can transmit the force generated by a shrinking MT to the membrane.

Next, we estimated the fraction of the contacts between the membrane and either MT shafts, growing MT ends or shrinking MT ends that led to successful membrane tubulation events occurring through sliding, TAC and dTAC mechanisms, respectively. In the absence of EB3, the fraction of successful events was similar for all three mechanisms

(Fig. 4g). This could be expected, because all events depended exclusively on the membrane-MT linkages mediated by His-GFP-SxIP that were not sensitive to the state of MT end or lattice. However, whereas the fraction of successful sliding and dTAC events was not affected by EB3, the fraction of successful TAC events was much higher in the presence of EB3 (Fig. 4g). This could be explained by EB3 preferentially concentrating at the growing MT ends, which in turn leads to a local increase in the SxIP accumulation (Fig 1c, Supplementary Fig. S1a).

EB3 and His-GFP-SxIP enhance membrane tubulation by the TAC complex

To analyze the contribution of EB3 and His-GFP-SxIP to the formation of membrane tubes, we examined the dynamics of these tubes. The interactions of GUVs with growing MT ends led to short (non-tubular) or long (tubular) membrane deformations (Fig. 5a,b, and Supplementary Video 5 and 6). These deformations retracted either because a MT depolymerized or because the membrane detached from the growing MT tip, similar to previous observations in cells[16, 20, 21] (Fig. 5a-c, Supplementary Fig. S3a, and Supplementary Video 5 and 6). The fraction of MT-membrane contacts leading to the formation of tubes was higher if both His-GFP-SxIP and EB3 were present in the assay, and was increased at a higher His-GFP-SxIP concentration (Fig. 4g and 5d). A higher concentration of His-GFP-SxIP also suppressed membrane tube detachment from MTs (Fig. 5d) and thus promoted formation of longer tubes. These data indicate that the increased abundance of the complexes formed by EB3 and His-GFP-SxIP at MT tips stimulates TAC-mediated membrane tubulation.

Modeling of membrane spreading driven by TAC formation

We next set out to obtain a quantitative description of the bilayer spreading process by combining theory with experimental measurements of different parameters of membrane-MT interactions (Table 1 and Supplementary Fig.S3b-l). We first described the membrane sliding mechanism using a simple analytical model[56, 57] (see Supplementary Notes for details). We assumed that the interaction between GUVs and MTs is dominated by the binding of the His-GFP-SxIP to MTs. We modeled the formation of a fixed-size membrane-MT adhesion domain, where we assumed a constant number of His-GFP-SxIP-MT connections at the tip of a membrane extension (Supplementary Fig. S4a). The interactions between His-GFP-SxIP and MTs were described by a binding rate $k_{on\text{-}m}$ and a detachment rate $k_{off\text{-}m}$, which were calculated from the experimentally measured mean maximum spreading speeds of sliding membrane tubes and the analysis of single molecule binding events of the His-SxIP-GFP to MTs (Table 1, Supplementary Fig. S3b,c,k). The detachment rate from a MT was expected to increase with the force $k_{off\text{-}m}(F_m)$ (ref. [58-60]), where F_m, the force needed to pull a tube from a GUV depended of the elastic modulus and the lateral tension of the GUV[61] (see equation S1 in Supplementary Notes). These values were measured by flickering spectroscopy (Table 1, Fig. 3g,h). In addition, we assumed that the membrane tension increased with tube length (see equation S2 in Supplementary Notes), and consequently, higher force was needed to keep a membrane tube extended when the tube length increased. The tip of the membrane deformation extended by a length of one tubulin dimer d=8 nm upon the formation of a new membrane-MT bond and decreased by the same distance if a bond at the membrane front was detached (Supplementary Fig. S4a and Supplementary Notes).

In this model the highest initial speed V of membrane spreading depends on the association rate $k_{on\text{-}m}$ and detachment rates $k_{off\text{-}m}(F_m)$ as

$$V=d[k_{on\text{-}m}-k_{off\text{-}m}(F_m)]$$

(Fig. 6a, Supplementary Fig. S3k; see equation S5 in Supplementary Notes). As the membrane tube increased in length, the force needed to pull a tube increases, and therefore the tube elongation rate slows down and finally drops to a value close to zero (Fig. 6a). This final state matches well the saturation regime observed experimentally (Fig. 6b, left panel).

To have a more realistic description of the tube elongation process that could be compared to experimental data, we next extended our simple model by taking into consideration the formation of bonds not only at the membrane tube tip but also all along the contact interface between the membrane deformation and a MT (Supplementary Fig. S4b and Supplementary Notes)[27]. The position of the adhesion molecules changed with time due to the diffusion of the His-GFP-SxIP on the membrane and along the MT lattice (Supplementary Fig. S3f-h). In addition, we included in the model changes in MT length to reflect MT dynamics. Finally, we incorporated into the model the EB3-induced enrichment of His-GFP-SxIP on MT tips compared to MT shafts (Supplementary Fig. S1a and Supplementary Fig. S3i,j), which leads to an uneven distribution of the kinetic parameters along the MT. Due to the fact that in this extended model a high number of reactions had to be considered, we performed *in silico* experiments using a stochastic approach[62, 63] (Supplementary Notes). When EB3 concentration was set to zero (Supplementary Fig. S4b), the predicted sliding speed overlapped quite well with the experimental data obtained by measuring the spreading rate of membrane tubes on MT shafts (Fig. 6b and Supplementary Fig. S3k,l). In addition, the estimated membrane spreading speeds from simulations and experiments were in agreement with the predictions of the analytical model, showing a decay which was dominated by tension (Fig. 6a-c and Supplementary Fig. S3k).

Our experimental data indicated that the formation of a TAC complex increased the probability of tubulation events and suppressed membrane detachment by promoting membrane association with MT tips (Fig. 5d). TAC formation can be regarded as the assembly of an extra EB3-dependent adhesion domain at the MT tip (Fig. 6c and Supplementary Fig. S4c). In the analysis of the *in silico* experiments, simultaneous movements of the membrane and MT tips were classified as TAC events, whereas other membrane spreading events were classified as sliding. Membrane tube retraction occurring independently of the MT tip was scored as a detachment event (Fig. 6c and Supplementary Fig. S3a). Similar to the experimental data (Fig. 4g), the fraction of successful sliding events observed in the simulations did not depend on the presence of EB3 (Fig. 6d).

The analytical model predicted that there was a certain maximum speed at which a membrane could slide along a MT (Fig. 6a and equation S5 in Supplementary Notes). Therefore, we expected that the TAC-driven membrane tubulation could be impeded at high MT growth rates. To test this hypothesis, we performed simulations and quantified the fractions of TAC events at different MT growth rates (Fig. 6e). The simulations predicted that the fraction of successful tubular deformations was approximately constant when MTs grew with a speed of 1-3 μm/min (Fig. 6e). When MT growth rates were increased, the system approached a transition region where the probability of tubular deformations rapidly decayed, indicating that the formation of the TAC complex was limited by the maximum sliding speed of the membrane. The inclusion of EB3 in the simulation increased the probability of TAC-mediated membrane tubulation at higher MT growth rates, because of a higher k_{on} and thus higher maximum spreading speed (Fig 6e).

We next investigated the match between our simulations and the experimental data, focusing on the TAC events. In the absence of EB3, the transition to low tubulation

probabilities was found at lower MT growth speeds than in the presence of EB3, indicating that EB3 enhanced the capacity of the membrane to follow the MT tip, in line with the predictions (Fig. 6e). We note that the *in silico* results matched the experimental data in the presence of EB3 better than in the absence of EB3 (Fig. 6e).

Since MT growth speeds in the presence of EB3 were always below the range where, according to the simulations, the transition to low tubulation probability occurred, we aimed to increase the MT growth speed in our assays. To achieve this, we added the human MT polymerase chTOG, since it has been shown that a combination of the frog homologue of chTOG, XMAP215, and the EB3 homologue EB1 strongly increased MT growth rate *in vitro*[64]. In the presence of chTOG, MT polymerization rate was indeed increased, whereas membrane tubulation probability was reduced, just as our simulations predicted (Fig. 6e). Taken together, these results support the idea that TAC formation is limited by MT growth rate.

We next combined simulations and experiments to estimate the forces that TACs could sustain. To do this, we performed stochastic simulations at different values of the force needed to pull a membrane tube[61]. We then estimated the probability of TAC formation and plotted it as the function of the force (Fig. 6f). To further compare simulations with experiments, we prepared GUVs with different values of the bending modulus by adding cholesterol, which makes membranes more stiff[47, 65, 66]. As expected[27, 29, 61], when the force required to make a tube increased, the probability of tubulation decreased. The estimated maximal force above which no tubes could be pulled by spreading was ~ 1.5-2 pN, depending on EB3 concentration, with the fraction of successful tubulation events at these forces being ~5%. At the same lipid composition and thus the same membrane rigidity, the presence of EB3, which promotes TAC assembly, increased the chances of pulling a tube both in the simulations and in the experiments (Fig. 6f).

Altogether, our simulations, which incorporate known physical effects related to membrane mechanics and force-dependent molecular detachment rates, and are based on experimentally measured parameters, provide a good quantitative explanation of the experimentally observed features of our *in vitro* reconstitution system.

Measurement of TAC-mediated force production

Since direct measurement of the force acting on a spreading membrane was challenging, we turned to other artificial cargos. First, we asked whether a quantum dot (Qdot) could be transported by adhesive interactions with growing MT tips without external load. We added streptavidin-coated Qdots in the presence of EB3 and a biotinylated version of the dimeric SxIP peptide (Bio-mCherry-SxIP) to a TIRFM assay in conditions previously identified to promote MT-driven membrane spreading (Fig. 7a). When both EB3 and Bio-GFP-SxIP were present, we observed Qdots travelling steadily with the growing MT tips (Fig. 7b, Supplementary Video 7). EB3 alone, without Bio-mCherry-SxIP, did not promote Qdot binding to MTs, while Bio-mCherry-SxIP alone promoted Qdot binding only to the MT shafts, but not to the tips (Fig. 7b). These results demonstrate that although EB proteins and their binding partners accumulate at MT ends by diffusion and exchange rapidly at MT tips[32, 33], a cluster of EB ligands can undergo processive EB-dependent motility on growing MT ends.

Next, we adapted the assay for direct measurement of the force sustained by TACs at growing MT ends. Neutravidin-coated glass beads were incubated with Bio-mCherry-SxIP and added to a chamber containing dynamic MTs, EB3 and Bio-mCherry-SxIP. A bead was optically trapped using low-power laser tweezers (stiffness ~0.005 pN/nm) and placed in front of a growing MT tip (Fig. 7c). Upon binding to a MT, the bead was initially pulled away from the trap center, and then gradually returned to zero position under

assisting load applied by the optical trap (Supplementary Video 8). We then used differential interference contrast (DIC) microscopy and high-resolution read-out from the quadrant photo detector (QPD) to ask whether the MT-bound bead continued its motion with the growing MT tip past the zero-force position against the opposing load applied by the optical trap. We found that when both EB3 and SxIP were present, the beads were displaced by growing MT tips past the zero position of the trap for seconds (Fig. 7d). This displacement lasted until a MT catastrophe, when the beads, which presumably retained their association with the MT tip, were pulled out of the trap by the force generated by MT shortening (Fig. 7d).

In the absence of EB3, the beads returned to zero-force position but did not continue to move steadily with the growing MT tip. Instead, we observed frequent and brief bead motions back and forth along the MT which continued when the MT tip grew past the position of the bead (Fig. 7e). These motions were clearly different from normal fluctuations of a trapped bead that was free from any interactions with MTs or glass (Fig. 7f). To quantify the effect of EB3 on the QPD signals, we measured the duration and the amplitude of the first positive bead displacement after the initial return to the zero position (Fig. 7g). Only forces above 0.1 pN (the resolution of our instrument) were quantified. We found that most events in the absence of EB3 were shorter than 1 s, while in the presence of EB3 they lasted for 15 ± 5 s (mean ± SEM, N = 24). The forces generated when both EB3 and Bio-mCherry-SxIP were present were in the range of 0.1-0.7 pN, while the forces observed without EB3 were significantly lower. Taken together, our data indicate that TAC formation allows growing MTs to exert adhesion-based forces in the range of 0.5 pN.

To measure the forces that are exerted by dTACs during MT shortening, we performed the same experiment using a much stiffer trap (0.03-0.05 pN/nm). In these conditions the forces in the direction of MT growth were barely distinguishable against the

bead's thermal fluctuations. However, forces in the direction of MT shortening did not result in the beads escaping the trap, as was observed for experiments with the soft trap (Fig 7d, Supplementary Video 8). Instead, the beads were pulled from the center of the optical trap by the shortening MT end, followed by detachment (Fig. 7h). We observed forces in the range of 2-10 pN that typically lasted for 0.2-2 s, independent of the presence or absence of EB3 (Fig. 7i). We have thus reconstituted EB3-dependent force coupling of TACs and EB-independent force coupling of dTACs.

Discussion

In this study we described a minimal system sufficient to reconstitute formation of long membrane tubes by three mechanisms: sliding, TAC and dTAC, all of which were previously described in cells[16, 20, 21, 24]. Previously, the sliding mechanism was attributed to motor proteins[20-22]. However, our data show that *in vitro*, membranes can spread on MT shafts independently of motors due to the adhesion mediated by a protein that can connect a lipid bilayer to MTs. Also TAC and dTAC events can be driven by a single MT- and membrane-binding protein, raising the question about the contribution of such biochemically simple mechanisms to shaping the ER and other membrane organelles in cells.

Although membrane tubes could form on dynamic MTs in the presence of a MT-binding peptide alone, the efficiency of membrane tubulation was strongly increased in the presence of EB3, to which the peptide could bind. Previous work in cells showed that the formation of the TAC complex requires the interaction between the SxIP-containing transmembrane ER protein STIM1 and EBs[21], but it remained unclear whether additional molecules are needed for membrane tubulation by this mechanism. Here, we showed that a combination of an EB protein and a membrane-associated SxIP partner is sufficient to

promote efficient membrane tube extension by growing MT ends. This mechanism relies on molecules that, unlike molecular motors, do not undergo processive motion, but rather concentrate at growing MT ends by a diffusion-based mechanism[32, 33]. In spite of their fast turnover, clustering of MT tip-tracking proteins on a specific structure, such as a bead or a membrane tip, is sufficient to bias the displacement of this structure and thus induce its processive motility. Importantly, EB3-dependent TAC mechanism was particularly important when MTs grew rapidly, and this likely explains its relevance in cells, where MTs grow with at a rate reaching 10-20 μm/min.

Furthermore, we observed that the presence of a protein with dual affinity to membranes and MT shafts was sufficient to pull membrane tubes by shrinking MTs (dTAC mechanism). Recent imaging work revealed dTAC-based ER remodeling in cells[24], and it was proposed that this mechanism employed factors different from those specific for TAC generation. However, our data show that the same molecules can in principle support both mechanisms. In fact, it is possible that any diffusible ER-resident protein with a strong affinity for MT lattices might be able to induce dTAC formation.

Our measurements indicated that in the conditions used, MT tip-localized EB3-SxIP complexes can mediate force generation in the range of ~0.5 pN. This value is in line with a recent study, which proposed that the interaction of a MT tip-bound EB protein with kinesin-14 can reverse the movement direction of this kinesin by exerting a force with a magnitude below 1 pN (ref. [67]). Based on the minimal value of tension and the membrane bending modulus measured by flickering spectroscopy, a force in the range of ~0.5 pN is sufficient to cause tubulation of membranes that are not under tension. However, based both on our simulations and experiments, the forces generated during TAC events when membranes were under some tension were estimated to be in the range of 1-2 pN. The discrepancy between this estimate and the force measurements at growing MT tips can be

attributed to the fact that the additional force is likely sustained by membrane adhesion along the MT lattice, whereas this contribution is absent in the bead-based assay. Furthermore, the membrane-MT interface, with the membrane partly wrapping around the MT cylinder, might lead to a higher number of contacts that together can sustain higher forces compared to a MT interface with a spherical bead. The forces generated by the combination of membrane-MT shaft interactions and the TAC complex are of the same order of magnitude as the forces generating membrane tubes by one-dimensional wetting[39]. Interestingly, the forces generated when the same MT-membrane connecting molecules are attached to shrinking MTs are an order of magnitude higher than those mediated by TACs, possibly because the attachment geometry is significantly different at depolymerizing ends.

To conclude, our data show that the three different mechanisms of MT-driven membrane tubulation can be explained by the formation of transient bonds between MTs and membranes, and that a biased self-spreading of the lipid bilayer on MTs can account both for the sliding and TAC mechanisms. MT-based membrane tubulation plays a major role in shaping the ER (ref. [3]) and is also important for the morphogenesis of other organelles, such as mitochondria[68] and recycling endosomes[69]. Since numerous non-motor MT-membrane linking proteins are known, they are likely to contribute to intracellular organelle organization through adhesion-based mechanisms described in this study.

Methods

Methods and the associated references are available in the online version of the paper.

Author Contributions

R.R.-G and V.A.V. designed and performed experiments and simulations, analyzed data and wrote the paper. M.P.L. and G.K. participated in developing the experimental setup, E.A.K. and L.C.K. contributed to data analysis and modeling, C.-Y. C., N.O., A.Ah., and M.O.S. contributed essential reagents. I.G. contributed to data collection and analysis, M.D and A.Ak. coordinated the project and wrote the paper.

Acknowledgements

We thank M. Monti for developing a first version of a model for MT plus end-dependent force generation. This work was supported by the European Research Council Synergy grant 609822 to M.D. and A.Ak., the EMBO long-term fellowships to R.R.-G. and a grant from the Swiss National Science Foundation 31003A_166608 to M.O.S.

Competing financial interests

The authors declare no competing financial interests.

References

1. Area-Gomez, E. & Schon, E.A. Mitochondria-associated ER membranes and Alzheimer disease. *Curr Opin Genet Dev* **38**, 90-96 (2016).
2. Fu, M.M. & Holzbaur, E.L. Integrated regulation of motor-driven organelle transport by scaffolding proteins. *Trends Cell Biol* **24**, 564-574 (2014).
3. Westrate, L.M., Lee, J.E., Prinz, W.A. & Voeltz, G.K. Form follows function: the importance of endoplasmic reticulum shape. *Annu Rev Biochem* **84**, 791-811 (2015).
4. Helfrich, W. & Servuss, R.-M. Undulations, steric interaction and cohesion of fluid membranes. *Il Nuovo Cimento D.* **3**, 137-151 (1984).
5. Helfrich, W. Elastic properties of lipid bilayers: theory and possible experiments. *Z. Naturforsch. C.* **28**, 693-703 (1973).
6. Zimmerberg, J. & Kozlov, M.M. How proteins produce cellular membrane curvature. *Nature Reviews Molecular Cell Biology* **7**, 9 (2005).
7. Jarsch, I.K., Daste, F. & Gallop, J.L. Membrane curvature in cell biology: An integration of molecular mechanisms. *Journal of Cell Biology* **214**, 375-387 (2016).
8. McMahon, H.T. & Boucrot, E. Membrane curvature at a glance. *Journal of Cell Science* **128**, 1065-1070 (2015).
9. Simunovic, M. *et al.* How curvature-generating proteins build scaffolds on membrane nanotubes. *Proceedings of the National Academy of Sciences* **113**, 11226-11231 (2016).
10. Dogterom, M., Kerssemakers, J.W., Romet-Lemonne, G. & Janson, M.E. Force generation by dynamic microtubules. *Curr Opin Cell Biol* **17**, 67-74 (2005).
11. Brouhard, G.J. & Rice, L.M. Microtubule dynamics: an interplay of biochemistry and mechanics. *Nat Rev Mol Cell Biol* **19**, 451-463 (2018).
12. Dogterom, M. & Yurke, B. Measurement of the force-velocity relation for growing microtubules. *Science* **278**, 856-860 (1997).
13. Grishchuk, E.L., Molodtsov, M.I., Ataullakhanov, F.I. & McIntosh, J.R. Force production by disassembling microtubules. *Nature* **438**, 384-388 (2005).
14. Garzon-Coral, C., Fantana, H.A. & Howard, J. A force-generating machinery maintains the spindle at the cell center during mitosis. *Science* **352**, 1124-1127 (2016).
15. Koshland, D.E., Mitchison, T. & Kirschner, M.W. Polewards chromosome movement driven by microtubule depolymerization in vitro. *Nature* **331**, 499-504 (1988).
16. Waterman-Storer, C.M., Gregory, J., Parsons, S.F. & Salmon, E.D. Membrane/microtubule tip attachment complexes (TACs) allow the assembly dynamics of plus ends to push and pull membranes into tubulovesicular networks in interphase Xenopus egg extracts. *J Cell Biol* **130**, 1161-1169 (1995).
17. McIntosh, J.R., Volkov, V., Ataullakhanov, F.I. & Grishchuk, E.L. Tubulin depolymerization may be an ancient biological motor. *J Cell Sci* **123**, 3425-3434 (2010).

18. Vale, R.D. The molecular motor toolbox for intracellular transport. *Cell* **112**, 467-480 (2003).

19. Powers, R.E., Wang, S., Liu, T.Y. & Rapoport, T.A. Reconstitution of the tubular endoplasmic reticulum network with purified components. *Nature* **543**, 257-260 (2017).

20. Waterman-Storer, C.M. & Salmon, E.D. Endoplasmic reticulum membrane tubules are distributed by microtubules in living cells using three distinct mechanisms. *Curr Biol* **8**, 798-806 (1998).

21. Grigoriev, I. *et al.* STIM1 is a MT-plus-end-tracking protein involved in remodeling of the ER. *Curr Biol* **18**, 177-182 (2008).

22. Woźniak, M.J. *et al.* Role of kinesin-1 and cytoplasmic dynein in endoplasmic reticulum movement in VERO cells. *Journal of Cell Science* **122**, 1979-1989 (2009).

23. Friedman, J.R., Webster, B.M., Mastronarde, D.N., Verhey, K.J. & Voeltz, G.K. ER sliding dynamics and ER–mitochondrial contacts occur on acetylated microtubules. *The Journal of Cell Biology* **190**, 363-375 (2010).

24. Guo, Y. *et al.* Visualizing Intracellular Organelle and Cytoskeletal Interactions at Nanoscale Resolution on Millisecond Timescales. *Cell* **175**, 1430 (2018).

25. Maurer, S.P., Fourniol, F.J., Bohner, G., Moores, C.A. & Surrey, T. EBs recognize a nucleotide-dependent structural cap at growing microtubule ends. *Cell* **149**, 371-382 (2012).

26. Honnappa, S. *et al.* An EB1-binding motif acts as a microtubule tip localization signal. *Cell* **138**, 366-376 (2009).

27. Campàs, O. *et al.* Coordination of Kinesin motors pulling on fluid membranes. *Biophysical journal* **94**, 5009-5017 (2008).

28. Shaklee, P.M. *et al.* Bidirectional membrane tube dynamics driven by nonprocessive motors. *Proc Natl Acad Sci U S A* **105**, 7993-7997 (2008).

29. Koster, G., VanDuijn, M., Hofs, B. & Dogterom, M. Membrane tube formation from giant vesicles by dynamic association of motor proteins. *Proc Natl Acad Sci U S A* **100**, 15583-15588 (2003).

30. Roux, A. *et al.* A minimal system allowing tubulation with molecular motors pulling on giant liposomes. *Proc Natl Acad Sci U S A* **99**, 5394-5399 (2002).

31. Leduc, C. *et al.* Cooperative extraction of membrane nanotubes by molecular motors. *Proc Natl Acad Sci U S A* **101**, 17096-17101 (2004).

32. Bieling, P. *et al.* Reconstitution of a microtubule plus-end tracking system in vitro. *Nature* **450**, 1100-1105 (2007).

33. Dragestein, K.A. *et al.* Dynamic behavior of GFP–CLIP-170 reveals fast protein turnover on microtubule plus ends. *The Journal of Cell Biology* **180**, 729-737 (2008).

34. Aher, A. *et al.* CLASP Suppresses Microtubule Catastrophes through a Single TOG Domain. *Dev Cell* **46**, 40-58 (2018).

35. Yamada, A. *et al.* Catch-bond behaviour facilitates membrane tubulation by non-processive myosin 1b. *Nat Commun* **5**, 3624 (2014).

36. Legland, D., Arganda-Carreras, I. & Andrey, P. MorphoLibJ: integrated library and plugins for mathematical morphology with ImageJ. *Bioinformatics* **32**, 3532-3534 (2016).

37. Feder, T.J., Weissmuller, G., Zeks, B. & Sackmann, E. Spreading of giant vesicles on moderately adhesive substrates by fingering: A reflection interference contrast microscopy study. *Phys Rev E Stat Phys Plasmas Fluids Relat Interdiscip Topics* **51**, 3427-3433 (1995).

38. Lobovkina, T. *et al.* Protrusive growth and periodic contractile motion in surface-adhered vesicles induced by Ca2+-gradients. *Soft Matter* **6**, 268-272 (2010).

39. Charles-Orszag, A. *et al.* Adhesion to nanofibers drives cell membrane remodeling through one-dimensional wetting. *Nat Commun* **9**, 4450 (2018).

40. Brochard-Wyart, F. & de Gennes, P.G. Adhesion induced by mobile binders: dynamics. *Proc Natl Acad Sci U S A* **99**, 7854-7859 (2002).

41. Bruinsma, R. & Sackmann, E. Bioadhesion and the dewetting transition. *Comptes Rendus de l'Académie des Sciences - Series IV - Physics-Astrophysics* **2**, 803-815 (2001).

42. Evans, E. & Rawicz, W. Entropy-driven tension and bending elasticity in condensed-fluid membranes. *Phys Rev Lett* **64**, 2094-2097 (1990).

43. Fournier, J.B., Ajdari, A. & Peliti, L. Effective-area elasticity and tension of micromanipulated membranes. *Phys Rev Lett* **86**, 4970-4973 (2001).

44. Sengupta, K. & Limozin, L. Adhesion of soft membranes controlled by tension and interfacial polymers. *Phys Rev Lett* **104**, 088101 (2010).

45. Cuvelier, D., Chiaruttini, N., Bassereau, P. & Nassoy, P. Pulling long tubes from firmly adhered vesicles. *Europhys. Lett.* **71**, 1015-1021 (2005).

46. Pecreaux, J., Dobereiner, H.G., Prost, J., Joanny, J.F. & Bassereau, P. Refined contour analysis of giant unilamellar vesicles. *Eur Phys J E Soft Matter* **13**, 277-290 (2004).

47. Rodriguez-Garcia, R. *et al.* Bimodal spectrum for the curvature fluctuations of bilayer vesicles: pure bending plus hybrid curvature-dilation modes. *Phys Rev Lett* **102**, 128101 (2009).

48. Bernard, A.L., Guedeau-Boudeville, M.A., Jullien, L. & di Meglio, J.M. Strong Adhesion of Giant Vesicles on Surfaces: Dynamics and Permeability. *Langmuir* **16**, 6809-6820 (2000).

49. Boulbitch, A., Guttenberg, Z. & Sackmann, E. Kinetics of membrane adhesion mediated by ligand-receptor interaction studied with a biomimetic system. *Biophys J* **81**, 2743-2751 (2001).

50. Cuvelier, D. & Nassoy, P. Hidden dynamics of vesicle adhesion induced by specific stickers. *Phys Rev Lett* **93**, 228101 (2004).

51. Volkov, V.A. *et al.* Centromere protein F includes two sites that couple efficiently to depolymerizing microtubules. *J Cell Biol* **209**, 813-828 (2015).

52. Grishchuk, E.L. *et al.* The Dam1 ring binds microtubules strongly enough to be a processive as well as energy-efficient coupler for chromosome motion. *Proc Natl Acad Sci U S A* **105**, 15423-15428 (2008).

53. Volkov, V.A., Huis In 't Veld, P.J., Dogterom, M. & Musacchio, A. Multivalency of NDC80 in the outer kinetochore is essential to track shortening microtubules and generate forces. *Elife* **7**, e36764 (2018).

54. Mitchison, T.J. Microtubule dynamics and kinetochore function in mitosis. *Annu Rev Cell Biol* **4**, 527-549 (1988).

55. Koshland, D.E., Mitchison, T.J. & Kirschner, M.W. Polewards chromosome movement driven by microtubule depolymerization in vitro. *Nature* **331**, 499-504 (1988).

56. Van Kampen, N.G. *Stochastic processes in physics and chemistry*, Vol. 1. (Elsevier, 1992).

57. Phillips, R., Theriot, J., Kondev, J. & Garcia, H. *Physical biology of the cell*. (Garland Science, 2012).

58. Bell, G.I. Models for the specific adhesion of cells to cells. *Science* **200**, 618-627 (1978).

59. Evans, E.A. & Calderwood, D.A. Forces and bond dynamics in cell adhesion. *Science* **316**, 1148-1153 (2007).

60. Erdmann, T. & Schwarz, U.S. Stability of adhesion clusters under constant force. *Phys Rev Lett* **92**, 108102 (2004).

61. Derényi, I., Jülicher, F. & Prost, J. Formation and interaction of membrane tubes. *Physical review letters* **88**, 238101 (2002).

62. Gillespie, D.T. Exact stochastic simulation of coupled chemical reactions. *The Journal of Physical Chemistry* **81**, 2340-2361 (1977).

63. Gillespie, D.T. Stochastic simulation of chemical kinetics. *Annu Rev Phys Chem* **58**, 35-55 (2007).

64. Zanic, M., Widlund, P.O., Hyman, A.A. & Howard, J. Synergy between XMAP215 and EB1 increases microtubule growth rates to physiological levels. *Nat Cell Biol* **15**, 688-693 (2013).

65. Rodríguez-García, R., Mell, M., López-Montero, I. & Monroy, F. Subdiffusive fluctuation dynamics of rigid membranes as resolved by ultrafast videomicroscopy. *EPL* **94**, 28009 (2011).

66. Arriaga, L.R. *et al.* Dissipative dynamics of fluid lipid membranes enriched in cholesterol. *Adv Colloid Interface Sci* **247**, 514-520 (2017).

67. Molodtsov, M.I. *et al.* A Force-Induced Directional Switch of a Molecular Motor Enables Parallel Microtubule Bundle Formation. *Cell* **167**, 539-552 (2016).

68. Kanfer, G. *et al.* CENP-F couples cargo to growing and shortening microtubule ends. *Mol Biol Cell* **28**, 2400-2409 (2017).

69. Delevoye, C. *et al.* BLOC-1 Brings Together the Actin and Microtubule Cytoskeletons to Generate Recycling Endosomes. *Curr Biol* **26**, 1-13 (2016).

70. Mathivet, L., Cribier, S. & Devaux, P.F. Shape change and physical properties of giant phospholipid vesicles prepared in the presence of an AC electric field. *Biophys J* **70**, 1112-1121 (1996).

71. Montenegro Gouveia, S. *et al.* In vitro reconstitution of the functional interplay between MCAK and EB3 at microtubule plus ends. *Curr Biol* **20**, 1717-1722 (2010).

72. Olieric, N. *et al.* Automated seamless DNA co-transformation cloning with direct expression vectors applying positive or negative insert selection. *BMC Biotechnol* **10**, 56 (2010).

73. Buey, R.M. *et al.* Sequence determinants of a microtubule tip localization signal (MtLS). *J Biol Chem* **287**, 28227-28242 (2012).

74. de Boer, E. *et al.* Efficient biotinylation and single-step purification of tagged transcription factors in mammalian cells and transgenic mice. *Proc Natl Acad Sci U S A* **100**, 7480-7485 (2003).

75. Gutierrez-Caballero, C., Burgess, S.G., Bayliss, R. & Royle, S.J. TACC3-ch-TOG track the growing tips of microtubules independently of clathrin and Aurora-A phosphorylation. *Biol Open* **4**, 170-179 (2015).

76. Mohan, R. *et al.* End-binding proteins sensitize microtubules to the action of microtubule-targeting agents. *Proc Natl Acad Sci U S A* **110**, 8900-8905 (2013).

77. Demchouk, A.O., Gardner, M.K. & Odde, D.J. Microtubule Tip Tracking and Tip Structures at the Nanometer Scale Using Digital Fluorescence Microscopy. *Cell Mol Bioeng* **4**, 192-204 (2011).

78. Seetapun, D., Castle, B.T., McIntyre, A.J., Tran, P.T. & Odde, D.J. Estimating the microtubule GTP cap size in vivo. *Curr Biol* **22**, 1681-1687 (2012).

79. Maurer, S.P., Bieling, P., Cope, J., Hoenger, A. & Surrey, T. GTPgammaS microtubules mimic the growing microtubule end structure recognized by end-binding proteins (EBs). *Proc Natl Acad Sci U S A* **108**, 3988-3993 (2011).

80. Schindelin, J. *et al.* Fiji: an open-source platform for biological-image analysis. *Nat Methods* **9**, 676-682 (2012).

81. Rodriguez-Garcia, R. *et al.* Direct Cytoskeleton Forces Cause Membrane Softening in Red Blood Cells. *Biophys J* **108**, 2794-2806 (2015).

82. Gittes, F., Mickey, B., Nettleton, J. & Howard, J. Flexural rigidity of microtubules and actin filaments measured from thermal fluctuations in shape. *J Cell Biol* **120**, 923-934 (1993).

83. Méléard, P., Faucon, J.F., Mitov, M.D. & Bothorel, P. Pulsed-Light Microscopy Applied to the Measurement of the Bending Elasticity of Giant Liposomes. *EPL* **19**, 267 (1992).

84. Hyman, A.A. Preparation of marked microtubules for the assay of the polarity of microtubule-based motors by fluorescence. *J Cell Sci Suppl* **14**, 125-127 (1991).

85. Sharma, A. *et al.* Centriolar CPAP/SAS-4 Imparts Slow Processive Microtubule Growth. *Dev Cell* **37**, 362-376 (2016).

86. Tinevez, J.Y. *et al.* TrackMate: An open and extensible platform for single-particle tracking. *Methods* **115**, 80-90 (2017).

87. Tarantino, N. *et al.* TNF and IL-1 exhibit distinct ubiquitin requirements for inducing NEMO-IKK supramolecular structures. *J Cell Biol* **204**, 231-245 (2014).

88. Benda, A. *et al.* How to determine diffusion coefficients in planar phospholipid systems by confocal fluorescence correlation spectroscopy. *Langmuir* **19**, 4120-4126 (2003).

89. Elson, E.L. & Magde, D. Fluorescence correlation spectroscopy. I. Conceptual basis and theory. *Biopolymers: Original Research on Biomolecules* **13**, 1-27 (1974).

90. Sorscher, S.M. & Klein, M.P. Profile of a focussed collimated laser beam near the focal minimum characterized by fluorescence correlation spectroscopy. *Review of Scientific Instruments* **51**, 98-102 (1980).

91. Rodriguez-Garcia, R. *et al.* The polarity-induced force imbalance in Caenorhabditis elegans embryos is caused by asymmetric binding rates of dynein to the cortex. *Mol Biol Cell*, mbcE17110653 (2018).

92. Widengren, J., Rigler, R. & Mets, U. Triplet-state monitoring by fluorescence correlation spectroscopy. *J Fluoresc* **4**, 255-258 (1994).

93. Gillespie, D.T. General Method for Numerically Simulating the Stochastic Time Evolution of Coupled Chemical Reactions. *Journal of computational physics* **22**, 403-434 (1976).

94. Nowak, S.A. & Chou, T. Models of dynamic extraction of lipid tethers from cell membranes. *Phys Biol* **7**, 026002 (2010).

95. Schnitzer, M.J., Visscher, K. & Block, S.M. Force production by single kinesin motors. *Nat Cell Biol* **2**, 718-723 (2000).

Figure legends

Figure 1. MT-driven formation of membrane tubes

(a) A scheme of the assay, which includes GUVs, GMPCPP-stabilized MT seeds, unlabeled tubulin, mCherry-EB3 and His-GFP-SxIP that binds to DOGS-NTA-Ni on the GUV surface.

(b) Confocal equatorial section of a GUV prepared from POPC (94.95%)/DOGS-Ni-NTA(5%)/Rh-PE(0.05%) and incubated with 15 nM His-GFP-SxIP. Scale bar: 2 μm.

(c) Three color TIRFM kymographs and snapshots, showing the accumulation of mCherry-EB3 (red) and His-GFP-SxIP (green) at the plus end of a growing MT (cyan) grown from rhodamine-tubulin labeled MT seeds. Kymograph scale bars: horizontal, 2 μm, vertical, 1 min. Snapshots, scale bar: 1 μm.

(d) Orthogonal view and surface render of a confocal Z stack obtained from a GUV after the incubation with dynamic MTs in presence of 200 nM mCherry-EB3 and 15 nM His-GFP-SxIP. Confocal Z stacks were obtained using spinning disk microscope. Scale bar: 5 μm.

(e) Left: Snapshot of a TIRFM time lapse movie illustrating GUV tubulation. Scale bar: 5 μm. Right: Normalized intensity profile of the boxed region shown in the snapshot images at the bottom. Scale bar: 2 μm.

Figure 2. Formation of long membrane tubes in the presence of dynamic MTs, EB3 and His-GFP-SxIP

(a) Representative images of a tubular network (red) observed at different concentrations of His-GFP-SxIP and 200 nM EB3. Each image is the maximum intensity projection obtained from 100 frames. Scale bar: 5 μm.

(b, c) GUV sphericity (b) and the total length of membrane tubes (c), measured at different His-GFP-SxIP and EB3 concentrations. Without EB3, 0 nM SxIP, n=16 GUVs; 5 nM SxIP, n=23 GUVs; 15 nM SxIP, n=16 GUVs. At 200 nM EB3, 0 nM SxIP, n=16 GUVs; 5 nM SxIP, n=57 GUVs; 15 nM SxIP, n=34 GUVs. Error bars indicate SEM.

(d) A diagram showing characteristic GUV shapes observed as a function of His-GFP-SxIP and EB3 concentrations. The numbers represent the proportion of tubular GUVs observed without EB3 at 0 nM SxIP, n=16 GUVs; 5 nM SxIP, n=23 GUVs; 15 nM SxIP, n=16 GUVs. At 200 nM EB3, 0 nM SxIP, n=16 GUVs; 5 nM SxIP, n=57 GUVs; 15 nM SxIP, n=34 GUVs.

(e) Still image of a GUV (red) in the presence of dynamic MTs (blue) and 200 nM His-EB3.

(f) Histogram of total length of membrane tubes (left) and GUV sphericity (right) measured at 200 nM of His-EB3 without His-GFP-SxIP, n=34 GUVs (red) and at 200 nM of mCherry-EB3 , 15 nM of His-GFP-SxIP, n=18 GUVs (blue).

Figure 3. Control of MT-dependent formation of tubular membrane networks by adhesion and tension

(a) Left: Schematic representation of different binding states of His-GFP-SxIP in the assay. Right: Snapshot of a TIRFM time lapse movie showing free MTs and MTs bound to a GUV. Only the His-GFP-SxIP and MT channels are shown. Scale bar: 5 μm.

(b) Averaged MT intensity profiles of the His-GFP-SxIP channel for MTs attached to a GUV (n = 6 movies 62 MTs), the region of the GUV close to the attached MT (n = 6, movies, 62 profiles) and free MTs (n=6 movies, 106 MTs). The values were normalized to the mean values of the MTs attached to a GUV.

(c) Snapshots of a TIRFM time lapse movie showing the development of a tubular membrane network over time. Scale bar: 5 μm.

(d) Averaged values of GUV sphericity as a function of time, normalized to the maximum experimental value. The shaded area represents SEM (n=11).

(e) Schematic representation of the two conditions where membrane fluctuations were investigated, GUVs in the presence of MTs and free GUVs. The equatorial and the bottom plane are indicated; blue lines represent MTs. The membrane fluctuates around an equilibrium position (undeformed state, yellow line) defined by the time-average of the GUV radius R_0. Fluctuations at each point (deformed state) are represented in grey and are defined by local deviations of the equatorial radius r_e from the average radius R_0.

(f) Phase contrast and fluorescence images of a GUV interacting with MTs. Bottom plane is shown on the left and center, equatorial plane is on the right. Scale bar: 5 μm.

(g) Experimental fluctuation spectrum calculated from the time-averages of quadratic fluctuation amplitudes of the equatorial modes, for free vesicles (red, n=39) and vesicles in contact with MTs (blue, n=13), as a function of the fluctuation mode *n*. The averaged curves were calculated after correcting each individual spectrum for pixelization noise and divided by $\pi\langle R_0\rangle^3/2$. The black dashed line represents the resolution limit, estimated by measuring the fluctuation spectrum of a fixed object in the focal plane. Shaded areas represent SEM.

(h) Estimated values of the bending modulus and lateral tension for free GUVs (n = 38) and GUVs in contact with MTs (n = 10). Error bars indicate SD.

Figure 4. Three mechanisms of MT-induced membrane tube formation

(a,c) Time lapse images of a membrane tube (red arrowheads) sliding along a MT (dashed yellow line) (a), or moving together with the plus end of a growing MT (white arrowheads) (c) in the presence of 200 nM mCherry-EB3 and 15 nM His-GFP-SxIP. Scale bar: 1 μm.

(b) Left: Kymograph of a membrane tube sliding along a MT and catching up with the MT tip (green arrowhead). Scale bars: horizontal, 2 min, vertical, 2 μm. Right: Speed of membrane sliding at 0 nM (n=9), and 200 nM (n=12) EB3 and 15 nM His-GFP-SxIP. Error bars indicate SD.

(d) The growth rate of free MTs (red) and MTs in contact with a membrane (blue), at the indicated EB3 and His-GFP-SxIP concentrations; n, from left to right: 63, 41, 179, 40, 41 and 67. Error bars indicate SD.

(e) Time lapse images of a membrane tube (red arrowhead) attached to the plus end of a depolymerizing MT (white arrowhead) (dTAC) in the presence of 15 nM His-GFP-SxIP without mCherry-EB3. Scale bar: 2 μm.

(f) The shortening rate of free MTs (red) and MTs pulling a membrane (blue), at the indicated EB3 and His- GFP-SxIP concentrations; n, from left to right: 36, 41, 58 and 73. Error bars indicate the SD.

(g) Fraction of successful membrane tube generation events occurring through different mechanisms at 15 nM of His-GFP-SxIP. The fraction of successful tubulation events was determined by dividing the number of observed tubes by the total number n of MT-membrane contacts that could potentially support a specific event (e.g. total number of MT-membrane contacts for sliding, membrane contacts with growing MTs for TACs and shrinking MTs for dTAC). 0 nM EB3:TAC (n=48 events, 7 experiments), dTAC (n=36 events, 5 experiments), sliding (n=50 events, 5 experiments). 200 nM EB3: TAC (n=68 events, 9 experiments), dTAC (n=6 events, 5 experiments), sliding (n=30 events, 5 experiments). Each black dot represents one experiment. The bars represent the mean value.

Figure 5. EB3 and His-GFP-SxIP contribute to TAC-mediated force generation

(a,b) Snapshots (top) and the corresponding kymographs (bottom) of a MT deforming a GUV at 50 nM mCherry-EB3 and 15 nM His-GFP-SxIP. GUV contours are shown by yellow lines. (a) The membrane detaches from the MT before developing a tubular shape. (b) The membrane remains attached to the MT tip during growth and shrinking phases. Scale bars: 5 μm (top panels), horizontal, 0.5 μm, vertical, 2 min (kymograph in (a)); horizontal, 2 μm, vertical, 2 min (kymograph in (b)).

(c) Snapshots (top) and the corresponding kymograph (bottom) of a TIRFM movie showing a membrane tube (red arrowheads) detaching from a MT tip (white arrowheads). Snapshot scale bar: (left) 5 μm, (right) 1 μm. Kymograph scale bar: vertical 1 μm, horizontal 1 min.

(d) Top: Fraction of successful membrane tube generation events. 0 nM EB3, n=50 events, 7 experiments; 200 nM EB3, n=68 events, 9 experiments, both in presence of 15 nM of His-GFP-SxIP. 200 nM EB3 and 5 nM of His-GFP-SxIP, n=37 events, 3 experiments. Bottom: fraction of detachment events from a MT tip. 0 nM EB3, n=50 events, 7 experiments; 200 nM EB3 n=68 events, 9 experiments, both in presence of 15 nM of His-GFP-SxIP; 200 nM EB3 and 5 nM of His-GFP-SxIP, n=37 events, 3 experiments. Data for the fraction of successful tubulation events in the presence of 15 nM His-GFP-SxIP are the same as in Fig. 4g and are included here for comparison. Error bars indicate SEM.

Figure 6. Modeling of membrane spreading and comparison of *in silico* and experimental data

(a) Predicted speed of membrane tip spreading along MT shafts as a function of time for three different values of the association rate using equation S5. Curves are averages of 100 individual traces with randomly sampled membrane parameters.

(b) Left and middle: Experimental and simulated tip positions of membrane tubes sliding along MTs. Different traces are indicated with different colors. Right: Average tube velocity as a function of time (blue), estimated from 60 stochastic simulations of membrane spreading on MTs. The shaded region represents SEM. Experimental values of the average tube velocity are shown with black dots; error bars represent SEM, n=12.

(c) Kymographs obtained from the stochastic simulations of membrane spreading in the presence of dynamic MTs.

(d) Fraction of successful sliding tubulation events, calculated from simulations in the same way as in Fig. 4g. EB3 0 nM, n=58 independent simulations (each represented by a black dot) and 1007 individual traces; EB3 200 nM, n=28 independent simulations and 348 individual traces. Error bars indicate SD.

(e) Fraction of membrane deformations becoming tubular as a function of MT growth rate for simulation and experiments. Data were normalized to the average fraction obtained at the lowest MT growth rate. The grey rectangles mark the areas where the probability decays with the speed. 0 nM EB3, n=50 events, 7 experiments; 200 nM EB3, n=68 events, 9 experiments; 50 nM EB3, n=28 events, 7 experiments without chTOG; n=22 events, 4 experiments at 30 nM of chTOG. Error bars indicate SEM.

(f) Fraction of membrane deformations becoming tubular as a function of the tube force. EB3 0 nM, n=59 independent simulations and 824 individual traces; EB3 200 nM, n=31 independents simulations and 424 individual traces. Error bars indicate SEM. The experimentally measured values are represented by rectangles due to the experimental uncertainty.

Figure 7. Cargo transport and force generation by growing and shrinking MT tips

(a) Schematics of the TIRFM experiment setup.

(b) Kymographs showing MTs polymerized from HiLyte-488 tubulin (cyan), bio-mCherry-SxIP and mCherry-EB3 (green) and Qdot705-streptavidin (red). Notation above the kymographs describes the experimental conditions. Scale bars: horizontal (5 μm), vertical (60 s).

(c) Setup of the optical trap experiments.

(d) An example of a QPD trace in the presence of EB3 showing the raw signal at 1 kHz (grey) and the signal after smoothing with a running average of 100 points (red). Images at the bottom show corresponding frames from the DIC video (Supplementary video 8). The red cross marks the centre of the optical trap. Scale bar: 5 μm.

(e) Analogous experiment in the absence of EB3. Bottom trace: the fast back and forth movements continued after the MT tip grew past the position of the trapped bead (white arrowhead). Scale bars: 5 μm.

(f) Example trace and image of a free, unattached bead in a trap. Scale bar: 5 μm.

(g) Force amplitude (left) measured at the growing MT tip, and force duration (right) in the presence (black, n = 24) or absence (red, n = 10) of 100 nM EB3. Horizontal line: median; box: 25-75%, whiskers: minimal and maximal values.

(h) Example trace of an SxIP-coated bead in the absence of EB3 pulled by a shortening MT tip showing the raw signal at 10 kHz (grey) and the signal after smoothing with a running average of 100 points (red).

(i) Force amplitude (left) measured at the shrinking MT tip, and duration (right) in the presence (black, n = 19) or absence (red, n = 22) of 100 nM EB3.

Methods

Preparation of vesicles

1-palmitoyl-2-oleoyl-glycero-3-phosphocoline (POPC), 1,2-dioleoyl-sn-glycero-3-[(N(5-amino-1-carboxypentyl)iminodiacetic acid)succinyl](nickel salt) (DOGS-Ni-NTA), 1,2-dioleoyl-sn-glycero-3-phosphoethanolamine-N-(lissamine rhodamine B sulfonyl) (ammonium salt) (Rh-PE), 1,2-dioleolyl-sn-glycero-3-phosphocoline (DOPC) and 1-oleoyl-2-{6-[(7-nitro-2-1,3-benzoxadiazol-4-yl)amino]hexanoyl}-sn-glycero-3-phosphocoline (NBD-PC) were purchased from Avanti Polar Lipids. Cholesterol was purchased from Sigma Aldrich. The lipid mixtures were composed of 94.95% POPC, 5% DOGS-Ni-NTA, 0.05% (Rh-PE/NBD-PC) or 94.95% DOPC, 5% DOGS-Ni-NTA, 0.05%Rh-PE. For experiments with cholesterol, the lipid mixture was 64.95% POPC, 5% DOGS-Ni-NTA, 0.05% Rh-PE and 30% Cholesterol (expressed as molar proportions). GUVs were prepared by electroformation[70] on two conductor indium tin oxide (ITO)-coated glass slides (Sigma Aldrich). Briefly, ten microliters of a lipid suspension (0.1 mg /mL) in chloroform were spread over the conductor surface. A chamber was made with non-adhesive silicone spacer (0.8 mm depth, Sigma Aldrich); after solvent evaporation the films were hydrated with sucrose solution (300 mM), and the electrodes were connected to an AC power supply (1V, 10 Hz) for 3.5 hours and (1.5V, 5 Hz) for 30 min to ensure good detachment of the GUVs from the ITO glass slides.

Protein purification

His-mCherry-EB3 was purified from *E. coli* as described previously[71]. mCherry-EB3 was cloned into a pET based bacterial expression vector with a N-terminal 6xHis tag followed by a 3C cleavage site using the restriction free positive selection method[72]. Protein production was performed in the *E. coli* expression strain Bl21(DE3) in LB broth by

inducing with 0.5 mM IPTG at an OD_{600} of 0.4 to 0.6 over-night at 20 °C. Cells were harvested by centrifugation at 4 °C, 3500 x g for 15 min and lysed by sonication in a buffer containing 50 mM HEPES, pH 8.0, 500 mM NaCl, 10 mM Imidazole, 10% Glycerol, 2 mM β-mercaptoethanol, and proteases inhibitors (Roche). The crude extracts were cleared by centrifugation at 20,000 x g for 20 min and the supernatants were filtered through a 0.4 micron filter before purification.

Protein purification was performed by immobilized metal-affinity chromatography (IMAC) on HisTrap HP Ni^{2+} Sepharose columns (GE Healthcare) at 4°C according to the manufacturer's instructions. The 6xHis tag was cleaved overnight by 3C protease during dialysis against lysis buffer (without proteases inhibitors). The cleaved sample was reapplied onto the IMAC column to separate the cleaved product from its tag and potentially uncleaved protein. Processed protein was concentrated and further purified on a HiLoad Superdex 200 16/60 size exclusion chromatography column (GE Healthcare) equilibrated in 20 mM Tris HCl, pH 7.5, 150 mM NaCl, 2 mM DTT. Protein fractions were analyzed by Coomasie stained SDS-PAGE. Fractions containing mCherry-EB3 were pooled and concentrated by ultrafiltration. Protein concentration was estimated by UV at 280 nm and the pure mCherry-EB3 was aliquoted, flash frozen in liquid nitrogen and stored at -80°C.

His-GFP-SxIP corresponds to the previously described construct, which includes EGFP, the two-stranded leucine zipper (LZ) coiled-coil domain of GCN4 and the C-terminal 43 residues of human MACF2 (MACF43)[26], which was cloned between *Nde*I and *Bam*HI sites of pET28a (Novagen, Merck Millipore, Billerica, MA, USA) and purified as described previously [73].

Bio-mCherry-SxIP was assembled by PCR amplification from mCherry with an N-terminal biotinylation tag (the peptide MASGLNDIFEAQKIEWHEGGG, which serves as a substrate

for the bacterial biotin-protein ligase BirA[74]), LZ and MACF43. Bio-mCherry-SxIP was cloned into pET28a vector linearized with *EcoRI* and *SalI* restriction enzymes. Protein purification was performed from BL21 DE3 cells. Expression was induced at OD 0.6 with 1 mM IPTG and continued overnight at 20ºC. After induction, bacteria were harvested by centrifugation. The supernatant was discarded and bacteria were resuspended in 5 ml/gram lysis buffer (50 mM Tris-HCl, pH 7.4, 300 mM NaCl, 1 mM dithiolthreitol (DTT), 0.5% Triton-X, Complete Protease Inhibitor and 0.2 mg/ml lysozyme.) After ~15 min incubation, cells were sonicated 5 times for 30 seconds with intervals of 1 min. The extract was pre-cleared by centrifugation at 20.000 x g for 45 minutes and the supernatant was incubated for 1 hr with Streptactin Sepharose beads (GE Healthcare) which had been washed 3 times in the lysis buffer. Next, beads were washed with a solution containing 2.5 mM D-biotin in the lysis buffer and spun down. The supernatant then incubated with Ni-NTA beads (Qiagen) for 1 hr. Subsequently, the beads were again spun down and washed with the elution buffer containing 50 mM Tris-HCl pH 7.4, 150 mM NaCl, 300 mM imidazole, 1 mM DTT, 0.1% Triton. Finally, a PD-10 desalting column (GE Healthcare) and a concentrator (Vivaspin MWCO 10K, Satorius) were used to perform buffer exchange. The protein was snap-frozen with 10% glycerol.

Human ch-TOG was purified from HEK293T cells using the Strep(II)-streptactin affinity purification. ch-TOG expression construct was based on a previously described construct[75] that was a gift of S. Royle (University of Warwick, UK). Ch-TOG was cloned into a modified pEGFP-N1 vector with a StrepII tag. HEK 293T cells were cultured in DMEM/F10 (1:1 ratio, Lonza, Basel, Switzerland) supplemented with 10% FCS, transfected using polyethylenimine (PEI, Polysciences) and harvested 2 days after transfection. Cells from a 15 cm dish were lysed in 500 µl of lysis buffer (50 mM HEPES, 300 mM NaCl and 0.5% Triton X-100, pH 7.4) supplemented with protease

inhibitors (Roche) on ice for 15 minutes. The supernatant obtained from the cell lysate after centrifugation at 21,000 x g for 20 minutes was incubated with 40 µl of StrepTactin Sepharose beads (GE) for 45 minutes. The beads were washed 3 times in the lysis buffer without the protease inhibitors. The protein was eluted with 40 µl of elution buffer (50 mM HEPES, 150 mM NaCl, 1 mM $MgCl_2$, 1 mM EGTA, 1 mM dithiothreitol (DTT), 2.5 mM d-Desthiobiotin and 0.05% Triton X-100, pH 7.4). Purified proteins were snap-frozen and stored at -80 °C.

In vitro reconstitution assays

In vitro assays with dynamic MTs were performed as described previously[76]. First double cycled GMPCPP MT seeds were prepared by incubating tubulin mix containing 70% unlabeled porcine brain tubulin (Cytoskeleton), 18 % biotin-tubulin(Cytoskeleton) and 12 % rhodamine-tubulin (Cytoskeleton) at a total tubulin concentration of 20 µM with 1 mM GMPCPP (Jena Biosciences) at 37° C for 30 minutes. MTs were pelleted by centrifugation in an Airfuge for 5 minutes and then depolymerized on ice for 20 minutes. After this step, a second round of polymerization at 37° C with 1mM GMPCPP was performed. MT seeds were pelleted as above and diluted 10 fold in MRB80 buffer (80 mM piperazine-N,N[prime]-bis(2-ethanesulfonic acid, pH 6.8, supplemented with 4 mM $MgCl_2$, and 1 mM EGTA) containing 10% glycerol, snap frozen in liquid nitrogen and stored at -80° C.

Flow chambers were assembled by sticking plasma-cleaned glass coverslips onto microscopic slides with a double sided tape. The chambers were treated with 0.2 mg/mL of PLL-PEG-biotin (Surface Solutions, Switzerland) in MRB80. After washing with the assay buffer MRB80, the chambers were incubated with 1 mg/mL NeutrAvidin (Invitrogen). Then 2-3 µL of MTs seeds were diluted in 80 µL of glucose 320 mM and attached to the biotin-NeutrAvidin links. The reaction mixtures supplemented with 20 µM of tubulin, 50 mM

KCL,0.1% Methyl cellulose,0.5 mg/mL k-casein, 1 mM GTP, an oxygen scavenging system (200 μg/mL catalase, 400 μg/mL glucose oxidase, 4mM DTT), and 100 nM of SiR-Tubulin (Cytoskeleton) was added to the flow chamber after centrifugation in an Airfuge for 5 minutes at 119,000 g. In the experiments with GUVs, the vesicles were added after centrifugation. The flow chamber was sealed with vacuum grease, and dynamic MTs with and without GUVs were imaged at 30°C using TIRF microscopy.

TIRF microscopy

TIRF microscopy was performed on an inverted microscope Nikon Eclipse Ti-E (Nikon) with a perfect focus system. The setup was equipped with a Nikon CFI Apo TIRF 100x1.49 N.A oil objective, Photometrics Evolve 512 EMCCD (Roper Scientific) or CoolSNAP HQ2 CCD camera (Roper Scientific) and controlled with the Metamorph 7.7.5 software. The final magnification was 0.063 µm/pixel, which includes the 2.5x magnification introduced by an additional lens (VM lens C-2.5x, Nikon). The temperature was controlled by a stage top incubator INUBG2E-ZILCS (Tokai Hit). The microscope was equipped with TIRF-E motorized TIRF illuminator modified by Roper Scientific France/PICT-IBiSa, Institut Curie. For excitation lasers we used 491 nm 100 mW Stradus (Vortan), 561 nm 100 mW Jive (Cobolt) and 642 nm 110 mW Stradus (Vortran). We used an ET-GFP 49002 filter set (Chroma) for imaging proteins tagged with GFP and NBD-PC lipid, an ET-mCherry 49008 filter set (Chroma) for imaging X-Rhodamine labelled tubulin ,Rh-PE lipid or mCherry-EB3 and an ET-405/488/561/647 for imaging SiR tubulin labelled MTs or Hilyte 647 porcine brain tubulin. We used sequential acquisition for triple-color imaging experiments.

Spinning disk microscopy

Spinning disk confocal microscopy was performed on a Nikon Eclipse Ti microscope equipped with a perfect focus system (Nikon), a spinning disk-based confocal scanner unit (CSU-X1-A1, Yokogawa, Japan), an Evolve 512 EMCCD camera (Roper Scientific, Trenton, NJ) attached to a 2.0X intermediate lens (Edmund Optics, Barrington, NJ), a super high pressure mercury lamp (C-SHG1, Nikon), a Roper scientific custom-ordered illuminator (Nikon, MEY10021) including 405 nm (100 mW, Vortran), 491 nm (100 mW, Cobolt) 561 nm (100 mW, Cobolt) and 647 nm (100 mW, Cobolt) excitation lasers, a set of BFP, GFP, RFP and FarRed emission filters (Chroma, Bellows Falls, VT) and a motorized stage MS-2000-XYZ with Piezo Top Plate (ASI). The microscope setup was controlled by MetaMorph 7.7.5 software. Images were acquired using Plan Fluor Apo VC 60x NA 1.4 oil objective. The 3D image reconstruction was carried out using Huygens Professional version 18.04 (Scientific Volume Imaging, The Netherlands).

Quantification of His-GFP-SxIP intensity along MTs

To build the average distribution of His-GFP-SxIP intensity at the MT tip (Supplementary Fig. S1a,c), we generated mean intensity profiles of 6 pixel (400 nm) thick lines with a length 2-3 µm along MTs, with the middle point positioned approximately at the MT tip[34, 77]. Previously[34], we extracted the fluorescence profile along a MT and fitted it with the error function, which determined MT tip position. Since the profile of His-GFP-SxIP intensity had a shape of a comet, fitting it to the error function was not possible (Supplementary Fig.1d). In order to use the error function to determine the position of MT tip, the maximum intensity from the His-GFP-SxIP peptide fluorescence profile was assigned to all preceding

points along the MT(Supplementary Fig. S1d)[78]. Then as described previously[34, 77], the intensity profiles *I(x)* were fitted with the error function shifted in *x* as:

$$I(x)=I_{BG}+\frac{1}{2}I_{AMP}\left(1+erf\left(\frac{x-x_c}{\sqrt{2}\alpha}\right)\right) \quad (1)$$

where I_{BG} corresponds to the intensity of background, I_{AMP} the amplitude of the fluorescent signal, x_c is the position of the MT tip and α the degree of tip tapering convolved with the microscope's point spread function. Each profile was shifted by its x_c value and background was subtracted. To generate the binding curve of the His-GFP-SxIP peptide (Supplementary Fig. S1b), profile intensities were measured at different EB3 concentrations on a single day with the same microscopy settings[79]. To estimate the mean His-GFP-SxIP intensity along the MTs (Fig. 3b), we generated mean intensity profiles of 6 pixel (400 nm) thick lines along whole MTs.

Analysis of the shape of tubular membrane network

To analyze the shape of a tubular network, we first generated a single image containing the maximum intensity projection of the time lapse movie using Fiji (Supplementary Fig. S1e)[80]. A custom MATLAB script was employed to segment the network using a supervised segmentation pipeline. Segmented images (Supplementary Fig. S1e) were used to measure the perimeter and the area using built-in MATLAB functions from the image processing toolbox. Sphericity was calculated by dividing the total area by the squared value of the perimeter[36]. The sphericity was normalized as:

$$Normalized\ sphericity=\frac{Sphericity\text{-}MIN\ (Sphericity)}{MAX(Sphericity)\text{-}MIN(Sphericity)}$$

where *max(sphericity)* and *min(sphericity)* were defined as the maximal and minimal value of the experimentally measured sphericity, respectively . Original segmented images were converted into nodes and branches (skeletonization) using built-in MATLAB functions. Skeleton representations of the networks were used to measure the total length of membrane tubes as the sum of the lengths of all detected branches (Supplementary Fig. S1e).

Analysis of thermal membrane fluctuations

Analysis of thermal fluctuations was performed as described previously [46, 47, 81]. GUVs were visualized using a phase contrast microscope (Nikon TE2000) with a 60x NA 1.4 oil objective. Fluctuations of the vesicle radius were measured at the equatorial plane by videomicroscopy. We acquired 1000 time lapse images of fluctuating GUVs. Each vesicle profile was digitalized and the GUV-equatorial fluctuations, namely $\delta R(x,t)=R_0-r_e(x,t)$ were measured as local deviations of the equatorial radius r_e at each point of the GUV contour from an average value, R_0 , where R_0 is calculated with respect to the center of mass of the GUV profile. The equatorial fluctuations were expanded in a series of discrete Fourier modes n as $\delta R(x,t)/R_0=\Sigma_q(a_q sin(qx)+b_q cos(qx))$, where a_q and b_q are the Fourier coefficients and $q=n/R_0$ (with n=2,3,…50). The series were truncated at n = 50.

The spectrum of the membrane fluctuations in the equatorial plane P_{eq} (in units of length^^{3}) by calculating time-averages of quadratic fluctuation amplitudes: $P_{eq}=A*(\langle|c_n|^2\rangle-\langle|c_n|\rangle^2)$, where $c_n^2=a_n^2+b_n^2$ and $A=\pi\langle R_0\rangle^3/2$ (Supplementary Fig. S1f, left). Since the amplitudes of the fluctuations estimated from experiments depended on the GUV mean radius $\langle R_0\rangle$, non-dimensional averaged curves were obtained after dividing each individual spectrum by $A=\pi\langle R_0\rangle^3/2$ (Fig. 3g and Supplementary Fig. S1f right)[46, 47]. The estimated

amplitude of the Fourier modes included errors due to the finite spatial resolution of the images (pixelization). This noise introduces in the fluctuations a systematic component, which could become dominant at high fluctuation modes[46, 82]. Consequently, the experimentally measured amplitudes were corrected by subtracting the noise as P_{eq} (corrected) = $P_{eq} - [(\pi\langle R_0\rangle^3/2)*\mathrm{var}(c_n)]$, where var($c_n$) represents the variance of c_n as explained in[46]. A detailed derivation of the formulas for error propagation is provided in the Appendix C of ref. [46]. In addition, we quantified the minimal fluctuation that we can estimate by measuring the fluctuation spectrum of a fixed object in the focal plane (Fig. 3g). As a model for a fixed object, we used a transparent circular disc of radius 10 μm, printed in a Quartz photomask coated with chrome (Toppan). Every fluctuation amplitude below the estimated resolution limit was discarded during fitting. A correction to account for to the finite integration time of the camera[46, 83] was also included in the analysis.

Mechanical parameters of the GUVs were obtained by fitting the experimental mode amplitudes to the theoretical spectrum for a planar membrane [46, 47]. Detection of the vesicle contours, post-processing and fitting procedures were carried out using a custom MATLAB script as described previously[47].

Analysis of MT and membrane dynamics

To analyze the dynamics of MTs and membrane tubes, kymographs were generated using Fiji (KymoResliceWide plugin, https://github.com/ekatrukha/KymoResliceWide). MT catastrophe frequency was determined as the ratio of the total number of catastrophes observed for a particular MT to the total time a MT spent growing. MT growth rate, as well as the speed of growing membrane tubes were determined manually from kymographs. To estimate the probability of tubular deformations and detachment events, we selected MTs growing beyond the visible contour of the GUV (Supplementary Fig. S3a) and divided the

number of observed tubular membrane deformations by the total number of MT growth events. To estimate the probability that a deformation stopped because the membrane tip detached from the MT tip, we divided the total number of detachment events by the total number of successful membrane deformations (Supplementary Fig. S3a).

To determine the spreading speed of a membrane tube, time lapse images of GUVs interacting with MTs were recorded at 3 s intervals with 200 ms exposure time for 5 or 10 min. Intensity profiles of membrane tubes labeled with Rh-PE were collected at different time points by averaging across 6-pixel (400 nm) wide lines. The position of a tube end was determined by fitting every profile with the error function using a custom written MATLAB script[77] (Supplementary Fig. S3l). Membrane tube spreading speed was calculated by differentiating the vector of the tube end position over time.

Reconstitution of Qdot transport with MT tips

Digoxigenin (DIG)-labelled tubulin was prepared as described previously[84]. All other tubulin products were purchased from Cytoskeleton. Chambers were prepared and imaged as described previously[53]. In brief, silanized slides and coverslips were assembled into chambers using double-sided tape and functionalized with anti-DIG IgG (Roche), then passivated with 1% Tween-20. Double-cycled, DIG-labelled GMPCPP-stabilized seeds were introduced, followed by the reaction mix containing 80 mM K-Pipes pH 6.9, 50 mM KCl, 1 mM EGTA, 4 mM $MgCl_2$, 1 mM GTP, 0.1% methylcellulose, 1 mg/ml κ-casein, 4 mM DTT, 0.2 mg/ml catalase, 0.4 mg/ml glucose oxidase, 20 mM glucose, 20 μM tubulin (5% labelled with HiLyte-488) and 30 pM Qdot705-streptavidin (Thermo Fischer) with or without the addition of 15 nM bio-mCherry-SxIP and 100 nM mCherry-EB3.

Images were acquired using Nikon Ti-E microscope (Nikon, Japan) with the perfect focus system (Nikon) equipped with a Plan Apo 100X 1.45 NA TIRF oil-immersion objective

(Nikon), iLas^2 ring TIRF module (Roper Scientific) and a Evolve 512 EMCCD camera (Roper Scientific, Germany). The sample was illuminated with 488 nm (150 mW for HiLyte488-tubulin), 561 nm (100 mW for mCherry-tagged proteins) and 642 nm (110 mW, for Qdot-705) lasers through a quad-band filter set containing a ZT405/488/561/640rpc dichroic mirror and a ZET405/488/561/640m emission filter (Chroma). Images were acquired sequentially with MetaMorph 7.8 software (Molecular Devices, San Jose, CA). The final resolution was 0.16 µm/pixel. The objective was heated to 34°C by a custom-made collar coupled with a thermostat, resulting in the flow chamber being heated to 30°C.

Optical trapping

1 µm glass beads functionalized with carboxy groups (Bangs Laboratories) were conjugated with PLL-PEG (Poly-L-lysine (20 kDa) grafted with polyethyleneglycole (2 kDa), SuSoS AG, Switzerland) supplemented with 10% v/v of PLL-PEG-biotin as described[53]. The bead surface was then saturated with Neutravidin and then Bio-mCherry-SxIP. Flow chambers were prepared as described above. Reaction mix contained 80 mM K-Pipes pH 6.9, 50 mM KCl, 1 mM EGTA, 4 mM $MgCl_2$, 1mM GTP, 1 mg/ml κ-casein, 4 mM DTT, 0.2 mg/ml catalase, 0.4 mg/ml glucose oxidase, 20 mM glucose and either 25 µM unlabelled tubulin with addition of 100 nM mCherry-EB3, or 10 µM unlabelled tubulin in the absence of EB3. Experiments were carried out at 25°C.

DIC microscopy and optical trapping were performed as described previously[53]. Measurements were performed at nominal trap power of 0.4W which resulted in a typical stiffness of 0.03-0.05 pN/nm. QPD signal was recorded at 10 kHz. For experiments measuring forces in the direction of the microtubule growth, which were expected to be in the sub-pN range, the 0.2W trap (the lowest setting for our instrument) was additionally softened down to 4-6 $\cdot 10^{-3}$ pN/nm using a circular polarizing filter placed in the wave path

of the trapping laser. QPD signal was recorded at 10 kHz and down-sampled to 1 kHz for analysis.

Single molecule measurements

His-GFP-SxIP single molecule binding events to MTs were recorded using TIRF microscopy (Supplementary Fig.S3b) as described previously[85]. Briefly, the assay was performed at 0.12 nM concentration of His-GFP-SxIP with high speed acquisition (50 ms/frame). 200 nM MCherry-EB3 was added as a tracer to detect MT plus ends. The number and dwell times of the binding events were extracted from kymographs that were generated using Fiji (KymoResliceWide plugin). The distributions of the dwell times were fitted with an exponential function, giving the dissociation rates from MT lattice and from MT tips (Supplementary Fig.S3c,d). The binding constant rate was determined by measuring the number of single molecule binding events per MT lattice length and assuming a length of 200 nm for the MT tip (Supplementary Fig.S3e).

The diffusion coefficient of His-GFP-SxIP on MT lattice D_{MT} was derived from the analysis of the mean square displacement (MSD) of single molecule spots diffusing along MTs[85](Supplementary Fig. S3b,f). Coordinates of diffusing spots were obtained and linked across frames using the Fiji plugin TrackMate[86]. MSD analysis was performed using MSDanalyzer MATLAB routine[87]. 25% of each MSD curve excluding zero was used for fitting. To compute the mean D_{MT} we only considered values where the coefficient of determination R^2 of the fitting was above 0.8 (n=95)(Supplementary Fig. S3f).

Fluorescence correlation spectroscopy

We used z-scan Fluorescence Correlation Spectroscopy (z-FCS) to measure the diffusion coefficient of His-GFP-SxIP bound to GUVs[88]. z-FCS measurements were performed with a Leica SP8 STED 3X microscope driven by LAS X and SymPhoTime (PicoQuant) software using a HC PLAPO 63x 1.2 NA water immersion objective. The sample was excited at 488 nm and time correlation was calculated at the time frequency of 600 kHz.

Confocal imaging was used to localize the top of the GUVs, starting from which a fast scan along the z-axis was performed. The position of the focus in z was set at 1 µm below or above of the plane with the maximum intensity. Afterwards, autocorrelation functions *G(t)* were measured at different positions along the z-axis in 0.2 µm steps. Three traces of 10 s duration were acquired at each position. The autocorrelation functions were fitted with the model considering one single species diffusing in 2 dimension described previously[89]:

$$G(t) = \frac{1}{N_p}\left(1+\frac{t}{t_D}\right)^{-1} \tag{2}$$

where N_p is the average number of particles in the confocal volume, t_D is the characteristic diffusion time and t is the lag time. The obtained average number of particles and diffusion times was plotted against the focus position z and fitted with the equations derived previously[90]:

$$t_D = \frac{w_0^2}{4D_m}\left(1+\frac{\lambda_0^2 \Delta z^2 t}{\pi^2 n^2 w_0^4}\right)^{-1} \tag{3}$$

$$N_P = \pi c w_0^2\left(1+\frac{\lambda_0^2 \Delta z^2 t}{\pi^2 n^2 w_0^4}\right)^{-1} \tag{4}$$

where w_0 is the radius of the beam in the focal plane, D_m is the diffusion coefficient of the protein bound to membrane, c is the average concentration in the illuminated area, n is the refractive index of the medium and λ is the wavelength of the excitation light.

We used FCS to estimate the probability of finding His-GFP-SxIP bound to EB3-bound MT tip as a function of the distance from the MT tip. We reconstituted MT plus-end tracking of the His-GFP-SxIP (15 nM) and EB3 (200 nM) as before, but in the absence of GUVs. When we performed FCS experiments, we observed peaks in the fluorescence intensity trace. (Supplementary Fig. S3i). The peaks represented His-GFP-SxIP-labeled MT ends[33, 91]. From the intensity values next to the intensity peak we calculated the autocorrelation function as described above. The autocorrelation function $G(t)$ was fitted using a triplet-state model for one fluorescent species [92] as follows:

$$G(t)=\frac{1}{N_p}\left[1-T+Te^{\left(\frac{t}{t_T}\right)}\right]\left(1+\frac{t}{t_D}\right)^{-1}\left(1+\frac{t}{t_D S^2}\right)^{-1/2} \quad (5)$$

where T is the triplet decay fraction, t_T is the lifetime of the triplet state, t_D is the diffusion time of the fluorescent species and S is the length-to-diameter ratio of the focal volume set to 4. We then estimated the mean of the maximum numbers of His-GFP-SxIP molecules at the MT tip $<N_{p\text{-}tip}>$ as:

$$<N_{p\text{-}tip}>=\frac{N_p<I_{peak}>}{<I_{solution}>} \quad (6)$$

where $<I_{peak}>$ is the mean peak intensity measured during 1 s (Supplementary Fig. S3i), and $<I_{solution}>$is the averaged intensity measured after the peak (Supplementary Fig. S3i). It was assumed that the intensity ratio was proportional to the ratio of the SxIP copy number. Considering a growth rate for MTs of ~ 2.8 μm/min we estimated that the maximum intensity recorded in 1 s corresponded to ~46 nm of the MT tip (~ 6 tubulin dimers). Since

EB3 binds to MTs between protofilaments at the interface between four tubulin dimers but not at the seam[25] we considered that within 6 dimer lengths of a 13 protofilament MT. Assuming that EB3 and SxIP interact at a ratio of 1:1, there were ~ 60 potential binding sites for His-GFP-SxIP. Considering that at 200 nM EB3 all EB3 binding site could be occupied, we estimated that the maximum probability of finding His-GFP-SxIP bound to EB3-bound MT tip was $<N_{p\text{-}tip}>/60=28/60=0.46$ (see Table1). Then we estimated the probability of His-GFP-SxIP binding along the MT length as the product of the maximum probability calculated above using normalized average His-GFP-SxIP intensity profiles measured by TIRF microscopy (Supplementary Fig. S1a).

Computer simulations

The simulations were implemented using the Gillespie algorithm for chemical reaction [63, 93]. A detailed description of the stochastic simulations and parameter values is provided in the Supplementary Notes and Table1. All the simulations were achieved in MATLAB using a custom routine. The computer code for simulations and analysis is available in https://github.com/RuddiRodriguez/Spreading;https://github.com/RuddiRodriguez/Spreading_membrane-MT_reaction_inside_EB

Data and software availability

All data that support the conclusions are available from the authors on request, and/or available in the manuscript itself. Data analysis was performed in MATLAB or using GraphPad Prism version 8.00 for (Mac OS X). The custom software used for data analysis and simulations in this manuscript can be found at https://github.com/RuddiRodriguez/; https://github.com/ekatrukha/KymoResliceWide. The software for the analysis of the GUVs

thermal fluctuations was developed M. Mell, I. López Montero and R. Rodríguez-García at the Complutense University in the group of F. Monroy and is available at https://github.com/RuddiRodriguez/programnnn. Schematic representations were generated in Adobe Illustrator with the support of ChemDraw (PerkinElmer Informatics) and Biorender (©BioRender - biorender.com)

Supplementary information

Legends to Supplementary Figures

Figure S1. Analysis of the distribution of His-GFP-SxIP along MTs.

(a) Averaged tip intensity profiles for His-GFP-SxIP in the presence of different EB3 concentrations and 20 μm of porcine tubulin. The shaded areas represent SEM. From low to high EB3 concentration, n=65, n=134, n=37, n=75, n=102, n=93.

(b) Averaged maximum His-GFP-SxIP fluorescence intensities at MT plus ends as a function of EB3 concentration. Data were normalized to the average maximum intensity obtained at the highest EB3 concentration. The color codes and n numbers are the same as in panel (a).

(c) Normalized averaged tip intensity profiles for His-GFP-SxIP along MTs at different times after the addition of GUVs. The profiles were normalized to the maximum intensity at time corresponding to the first movie acquired after the addition of the GUVs (t=0). t=0, n=17; t=10min, n=25; t=20min, n=18.

(d) Top: Snapshot of a TIRFM time lapse movie. Scale bar: 1 μm. Bottom: MT tip intensity profile (red dots) and the same profile after the maximum intensity was assigned to each of the preceding points along the MT (blue dots). The transformed profile was fitted with the error function (black line). Figure illustrated position fitting for consecutive the intensity profiles averaging in Fig. S1a,c.

(e) Left: Snapshot of a tubular membrane network. The image is the maximum intensity projection obtained from 100 frames of time lapse images. Center: Segmented tubular network. Right: Skeletal representation of the tubular network. Scale bar: 5 μm.

(f) Experimental fluctuation spectrum calculated from the time-averages of the quadratic fluctuation amplitudes of the equatorial modes (red dots) measured for a single GUV with a radius of 10 μm. The blue line is the systematic contribution of the pixelization noise to

the experimental fluctuation amplitude, which increases with the mode *n*. The black dots are the amplitudes of fluctuations corrected for the pixelization noise. (Right) the spectrum was normalized by the factor $A=\pi\langle R_0\rangle^3/2$. Error bars represent SE.

Figure S2. **Three mechanisms of MT-induced membrane tube formation**

(a,b,c) Time lapse images of a membrane tube moving along a MT shaft (sliding, a); together with the plus end of a growing MT (TAC, b) or by attachment to the plus end of a depolymerizing MT (dTAC, c). Scale bar: 2 μm.

Figure S3. Determination of parameters used for stochastic simulations.

(a) Schematic representation of different membrane deformations induced by dynamic MTs.

(b) Kymographs of dynamic MTs grown in presence of 0.2 nM His-GFP-SxIP and 200 nM of mCherry-EB3.

(c-d) Histograms of dwell time of single His-GFP-SxIP molecules at MT lattice (c) and growing MT plus ends (d); experimental conditions were the same as in panel (c). The red lines represent monoexponential fits.

(e) Association rate of the His-GFP-SxIP on MT lattice and growing MT plus ends, expressed in number of binding events per length.

(f) Mean square displacement (MSD) for single His-GFP-SxIP molecules diffusing on MT lattice.

(g) Representative autocorrelation function obtained from the diffusion of the membrane-bound His-GFP-SxIP molecules.

(h) Diffusion time of the membrane-bound His-GFP-SxIP molecules measured by FCS as a function of the position in z.

(i) Representative intensity time trace of a MT tip labeled with EB3-GFP recorded by FCS. The inset shows maximum intensity during a time window of 12 s. The grey rectangle marks the intensity in 1 s.

(j) Estimated occupational probability of His-GFP-SxIP at the MT tip in the presence of 200 nM EB3.

(k) Comparison between curves representing the speed of membrane tube sliding along MT lattice modelled using different association rates and the experimentally determined membrane sliding speeds.

(l) Membrane tip intensity profile at different time points measured from a GUV sliding along a MT shaft in presence of 15 nM of His-GFP-SxIP without EB3. The position of the membrane moving along a MT shaft was determined from the fitting of the intensity profiles to the step function.

Figure S4. Scheme illustrating the analytical model and stochastic simulations.

(a) Kinetic scheme for the one-step model.

(b,c) Kinetic schemes for the simulations of a membrane sliding along a MT shaft and at the MT tip in the presence of EB3.

Legends to Supplementary Videos

Video 1. **Membrane tubes growing from a GUV in the presence of MTs.** Images of Rh-PE (red, membrane), GFP (green, His-GFP-SxIP), mCherry-EB3 (red) and SiR (cyan, MT) tubulin were acquired sequentially using TIRFM at with a 3 s interval. The movie is displayed at 5 fps. Scale bar: 5 μm.

Video 2. **Membrane tube sliding along a MT.** Images of Rh-PE (red, membrane), GFP (green, His-GFP-SxIP), mCherry-EB3(red) (left) and SiR tubulin (MT) (right) were acquired sequentially using TIRFM at with a 3 s interval. The movie was displayed at 5 fps. Scale bar is 2 μm.

Video 3. **Membrane tube extending together with a growing MT plus end.** Images of Rh-PE (red, membrane), GFP (green, His-GFP-SxIP), mCherry-EB3 (red) (left) and SiR tubulin (MT) (right) were acquired sequentially using TIRFM at with a 3 s interval. The movie is displayed at 5 fps. Scale bar: 2 μm.

Video 4. **Membrane tube pulled by a depolymerizing MT.** Images of Rh-PE (red, membrane) and GFP (green, His-GFP-SxIP) (left) and SiR tubulin (MT) (right) were acquired sequentially using TIRFM at with a 3 s interval. Note the strong accumulation of the His-GFP-SxIP at the tip of the membrane deformation. The movie is displayed at 5 fps. Scale bar: 2 μm.

Video 5. **Membrane tube growing and retracting together with a MT plus end.** Images of Rh-PE (red, membrane), mCherry-EB3 (red) and SiR tubulin (cyan, MT) were acquired sequentially using TIRFM at with a 3 s interval. The movie is displayed at 5 fps. Scale bar: 3 μm.

Video 6. Extension and retraction of MT-dependent non-tubular GUV deformations. Images of Rh-PE (red, membrane), mCherry-EB3 (red) and SiR tubulin (cyan, MT) were acquired sequentially using TIRFM at with a 3 s interval. The movie is displayed at 5 fps. Scale bar: 3 μm.

Video 7. **Qdot transport with the tip of the growing MT**. Three channels were imaged by TIRFM sequentially at 1.3 s interval: Qdot705-streptavidin (red), HiLyte488-tubulin (cyan), Bio-mCherry-SxIP (15 nM, green) and mCherry-EB3 (100 nM, green). The

corresponding kymograph is shown in Fig 7b. The movie is displayed at 30 fps. Scale bar: 5 μm.

Video 8. **A growing MT end pushes a trapped glass bead**. A 1 μm glass bead coated with bio-mCherry-SxIP trapped in a soft trap was imaged using DIC microscopy at 8 fps and every 10 frames were averaged. The movie is displayed at 30 fps. The QPD trace corresponding to this experiment is shown in Fig 7e.

Supplementary notes

Physical modeling

Membrane sliding along MT lattice

To describe membrane sliding along MT lattice, a minimal one dimensional (1D) theoretical model was adapted from a previous publication[49]. We considered that the binding-unbinding reaction of His-GFP-SxIP to MT takes place in the close vicinity of the tip of a membrane deformation. The width of the reaction zone d in the 1D model was fixed to the length of one tubulin dimer, d = 8 nm. Moreover, we considered a reaction-dominated regime because of the high His-GFP-SxIP concentration at the GUV-MT interface (Fig. 3a,b). For simplicity, we first considered only the tip of the tube that extended for a distance L. We assumed that the tip moves in a biased-random walk, stepping from one binding site to the next with forward rate $k_{on\text{-}m}$ and backward rate $k_{off\text{-}m}$. The unbinding rate depends on the force barrier $F_m(t)$ to pull a membrane tube as described previously[27].

$$k_{off\text{-}m}(F_m) = k_{off\text{-}m} * exp\left[\frac{F_m(t)\xi}{k_B T}\frac{1}{n_p}\right] \tag{S1}$$

where $F_m(t)=2\pi(2\sigma(t)\kappa)^{1/2}$ (ref. [61]), κ is the bending modulus and $\sigma(t)$ is the lateral tension of the membrane. The parameter ξ is the characteristic length of the potential barrier between bound and unbound states, T is the temperature, k_B the Boltzmann's constant and n_p is the number of peptides bound at the tip. At the tip, the load is equally distributed between all the bonds due to the parallel organization (Supplementary Fig. S4a). The lateral tension of a flaccid membrane with initial tension σ_0, increased during tube elongation as [45]:

$$\sigma(t)= \sigma_0 * exp\left[\frac{8\pi\kappa}{k_B T}\alpha\right] \quad \text{(S2)}$$

where $\alpha= A/(A-A_0)$ is the relative area change of the GUV during tube elongation, $A_0=4\pi R^2$ is the initial area of the GUV, R the GUV radius and $A_0=2\pi r_0 L(t)$ is the area of the cylindrical tube; r_0 is the curvature radius of the tether and $L(t)$ the tether length. Based on the considerations above, we described the dynamics of a sliding membrane with a one-point one-step master equation[56, 57]. The probability that the tip of a sliding membrane ends up at the site n on the MT lattice at the time $t+\Delta t$ starting from the time t is the sum over all of the individual paths available to the system with the condition that the final state is fixed to one and can be written as:

Stepping forward Stepping backward Stay at site n

$$p(n,t+\Delta t)= k_{on-m}\Delta t p(n-1,t)+k_{off-m}(F)\Delta t p(n+1,t)+(1-k_{on-m}\Delta t-k_{off-m}(F)\Delta t)p(n,t) \quad \text{(S3)}$$

We transformed this equation into the more familiar continuum form as the function of the position x along the MT lattice, where the probability $p(x,t)$ for finding the tip of the deformation at position x is equal to $p(n,t)$ when $x=nd$ as was done in [57]. This led to a result that represents a biased diffusion equation for the front of the sliding membrane of the deformation tip:

$$\frac{\partial p}{\partial t}=-V\frac{\partial p}{\partial x}+D\frac{\partial^2}{\partial x^2} \quad \text{(S4)}$$

where

$$V=d[k_{on-m}-k_{off-m}(F_m)] \quad \text{(S5)}$$

and

$$D=\frac{d^2}{2}[k_{on\text{-}m}+k_{off\text{-}m}(F_m)] \quad \text{(S6)}$$

V is the average speed of the membrane tip and *D* is the variance of the tip position due to the stochastic nature of the process. As can be seen from Eq. (S5), V depends on $F(L)$ or, in the context of tip's probability function *p*, ultimately on *x*. To generate the dependence of speed for different time points of spreading (depicted in the Figure 6a and Supplementary Fig. S3k), we used iterative estimation of $x(t)$ over time series with step Δt:

$$x_{n+1}((n+1)\cdot\Delta t)=x_n(n\Delta t)+V_n(x_n)\Delta t \quad \text{(S5a)}$$

with the initial condition $x(0)=0$, which at the end provided values of V_n for each time point $n\ \Delta t$. We chose the value of Δt = 0.5 s, and the variation in this parameter in the range of 0.1-5 s did not affect the final result. Curves in Fig.6a are averages of multiple solutions of (S5a) with random values of GUVs physical parameters from Eqs. (S1)-(S2) described in the next section.

Parametrization of the model

We assumed that the affinity of the membrane for the MT is determined by the binding properties of the His-GFP-SxIP to MT. The value of the $k_{off\text{-}m}$ = 1.7 s^{-1} was defined as the inverse of the dwell time of the His-GFP-SxIP on the MT lattice, obtained from the analysis of the His-GFP-SxIP single molecule binding events (Supplementary Fig. S3b-e). We generated the curves in Figure 6a with three different values of $k_{on\text{-}m}$ = (8,16,26)s^{-1}. In our model, only $k_{off\text{-}m}$ was modified by the force required to pull a membrane tube as described by Eq. S1 and S2.

The mechanical parameters of the membrane were obtained from the analysis of thermal fluctuations of the GUVs (Fig. 3g). The precise value of the characteristic length of the potential barrier ξ between bound and unbound states is unknown for our system.

However, the values reported in different systems are in the range between 1-2 nm [94, 95]. For modeling, we fixed ξ to 1 nm.

The radius of curvature of the deformation r_0 defines the number of SxIP molecules bound to the tip. In the 1D model r_0 was represented by a fixed length $L=dn_p$ in the range between 8 and 32 nm (ref. [27]). For modeling, the number of SxIP molecules bound to the tip was randomly selected between 1 and 3.

The curves in Fig. 6a are the average of 100 individual traces. For each simulation, the lateral tension and the bending modulus of the simulated membrane were randomly sampled from a normal distribution with the mean and variance obtained from the analysis of the thermal fluctuations of the GUVs (Fig. 3g). The radius *R* was sampled from a uniformly randomly distributed values ranging between 5 and 15 µm.

Stochastic simulations

Membrane sliding along MT lattice

To simulate the dynamics of membrane tubes sliding along MTs, we have adapted the previously developed model for motors pulling fluid membranes[27]. His-GFP-SxIP molecules were represented by particles. MTs were represented by a discrete one-dimensional (single protofilament) lattices with *M* grid cells numbered from left to right (from the seed to plus end), and the membrane was described by a one-dimensional discrete lattice with *N* grid cells with $N<M$, also numbered from left to right (Supplementary Fig.S4b). The condition $N<M$ guaranteed that the substrate for the adhesion was always available. Lattice spacing was fixed to the size of a tubulin dimer d=8 nm. Individual MT cells were considered attachment sites with capacity of 1 molecule and individual membrane sites were reservoirs of SxIP molecules. The number of SxIP molecules in a

given cell at the MT grid represented the MT occupation number n_{MT}. Similarly, the number of SxIP molecules occupying each site on the membrane was denoted as the membrane occupation number n_m. Along the MT, SxIP molecule attachment sites were either empty (n_{MT}=0) or occupied (n_{MT}=1). We restricted the number of SxIP molecules attached to the MT at a given site to 1. However, along the membrane, each cell in the grid was unoccupied or occupied by several SxIP molecules.

The specified transitions of the SxIP molecules attached to a MT were:

1. Detachment from the MT with a rate $k_{off\text{-}m}$. If the transition occurred at the tip of the deformation, the tube retracted to the next site containing a bound SxIP molecule.
2. Diffusion to the left or to the right with a rate $k_{D\text{-}MT}$, if the site was empty.
3. Diffusion to the right from position *N* was not allowed.
4. Diffusion to the right from position 1 increased the number of peptides in the deformation by one.

The putative transitions of the SxIP molecules detached from a MT were:

5. Attachment to the MT with a rate $k_{on\text{-}m}$ if the site on the MT was unoccupied. If the transition happened at the tip, the deformation was extended by one site.
6. Diffusion to the left or to the right with a rate $k_{D\text{-}M}$ if the site was empty.

In the particular case of a membrane spreading along a MT lattice, the on-off rates along the deformation remained constant; however, at the tip of the deformation, the dissociation rate depended on the force barrier as explained above (see eq. S1).

Membrane spreading at the tips of growing MTs

The stochastic simulations describing the behaviour of spreading membrane tubes in the presence of dynamic MTs included some additional features. As before, the MT was represented by a discrete 1D lattice, but with *N* grid cells numbered from left to right and the membrane was described by a discrete 1D lattice with *M* grid cells (Supplementary Fig.S4c). A feature of the simulation in the presence of growing MTs was the stochastic dynamics of the MTs. In the reaction scheme for MTs that was used in the simulations, MTs could be either in a growth phase or in a shrinkage phase.

For a MT in the growth phase, the possible events were:

1. Association of a tubulin dimer at position *N*: The length of the MT was increased by one dimer. The length of the tube was unchanged.
2. Dissociation of a tubulin dimer at position *N*: The length of the MT was decreased by one dimer. If the membrane was spreading up to the tip (M=N), it would also shrink to the next site containing a bound SxIP molecule.
3. Catastrophe: A change in the state from the growth phase to the shrinkage phase.
4. Rescue: A change in the state from the shrinkage phase to the growth phase.

The specified transitions of the SxIP molecules attached and detached from a MT were as before with the following special rule for SxIP molecules detached from a MT:

5. Attachment to the MT with a rate $k_{on\text{-}m}$ if the site on the MT was unoccupied. If the transition happened at the tip of the membrane, the deformation was extended by one site. If the membrane was spreading up to the tip (M=N) the transition was not allowed, because in our experiments, the membrane was never observed to spread beyond the MT tip.

As before, the dissociation rate was constant along the MT, but in the vicinity of the deformation tip, the rate depended on the force barrier. The association rate was regulated in space and time by the presence or lack of EB3.

Boundary between the deformation and the vesicle

Position 1 in the grid characterized the connection of the deformation with the GUV[27] and constituted the only source of SxIP molecules entering the membrane tether. We assumed that there is no influx of free SxIP molecules from solution. Since the linear density of SxIP molecules in the deformation must be constant over time, at this position the occupation numbers of the attached and detached molecules were kept constant and equal to 1 (n_{MT}=n_m=1). Diffusion from site 2 to 1 was not allowed, to keep the number of molecules in the deformation constant over time. The diffusion rate of the peptides that were not attached to the MT at position 1 was different from the other sites in the grid and was defined as

$k_{D\text{-}M1=}\rho_{SxIP}*V_{tube}$, where ρ_{SxIP} is the linear density of the SxIP molecules in the deformation and V_{tube} is the growth speed of the tube. This condition accounted for the influx of molecules entering the deformation due to the membrane flow resulting from the tube growth.

Density of SxIP molecules in the stochastic simulation

At the beginning of the simulation, the linear density of the SxIP molecules was estimated as described previously[27]: $\rho_{SxIP\text{-}linear}= \rho_{SxIP\text{-}Dlinear}+ \rho_{SxIP\text{-}Alinear}$, where $\rho_{SxIP\text{-}Dlinear}$ and $\rho_{SxIP\text{-}Alinear}$ were the linear density of the SxIP molecules detached and attached to the MT respectively. The linear density were defined as: $\rho_{SxIP\text{-}Dlinear}=2\pi r_0 \rho_{SxIP\text{-}MT} (k_{off\text{-}m} /(k_{off\text{-}m} + k_{on\text{-}}$

$_m$)) and $\rho_{SxIP\text{-}Alinear}=2\pi\, r_0\, \rho_{SxIP\text{-}MT}\, (k_{on\text{-}m} /(k_{off\text{-}m} + k_{on\text{-}m}))$, $\rho_{SxIP\text{-}MT}$ was the surface density of SxIP molecules at GUVs surface in contact with MTs estimated experimentally, and r_0 was the curvature radius of the deformation.

Gillespie algorithm: first-family method

The system was characterized by a rate matrix $k_{S,,F}$ where $S=1,\ldots N$ indicates the sites in the 1D lattice representation and $F=1,\ldots 11$ the number of potential transitions of the SxIP molecules. To implement the first-family method, we considered every transition F as a family with S potential reactions in each family[63]. Every family F is then considered as a pseudoreaction with the stochastic rate $a_0^F \equiv \sum_{j=1}^{S} k_j^F * n_s$, where k_j^F is the rate of the family F and n_s=(n_m or n_{MT}) is the occupation number at the position S. To generate the time t to the next reaction event and the index pair (F,S) that identifies the type of transition and the position, we generated F+1 random numbers $r_1,\ldots r_{F+1.}$ We used the first F numbers to calculate

$$t_F=\frac{1}{a_0^F} ln\left(\frac{1}{r_F}\right) \quad (F=1,\ldots 11) \tag{S7}$$

then

$$t=\min(t_F)$$
$$F=\text{the index of the smallest } t_F \tag{S8}$$

From the above, we determined the type of the next transition (detachment, attachment, diffusion, MT polymerization, MT depolymerization and MT transitions between growth and shrinkage). The position S of the transition in the grid was determined as:

$$S = min, m \in N, \text{ s.t. } \sum_{m=1}^{m} a_S^F > r_{F+1} a_0^F \sum_{m=1}^{m} a_S^F > r_{F+1} a_0^F \qquad \text{(S9)}$$

where $a_S^F = k_S^F * n_s$ and k_S^F is the rate of the family F at position S on the grid.

Simulation parameters in the absence of EB3

As before, the value for $k_{off\text{-}m}$ = 1.7 s^{-1} was defined as the inverse of the dwell time of His-GFP-SxIP molecules on MT lattice, obtained from the analysis of the single molecule binding events (Supplementary Fig. S3b,c). The stochastic rate of the detachment reaction was $a_{off\text{-}m} = k_{off\text{-}m} * n_{MT}$. As explained above, the dissociation rate remained constant along the MT, but was allowed to change at the very end of a membrane deformation. The first n_p SxIP molecules bound to the MT at the tip of a deformation shared the force to pull a tube. The parameter n_p was determined as a value of membrane occupancy n_{MT} of the last four right elements. The parameters σ_0, κ and R were random variables sampled from a normal distribution. The parameter ξ was fixed to 1 nm.

To determine the value of $k_{on\text{-}m}$ we compared the results obtained from the one-step model using different values for $k_{on\text{-}m}$ (Fig. 6a and Supplementary Fig. S3k). Based on the experimental data (Supplementary Fig. S3k), we found that $k_{on\text{-}m}$=16 s^{-1} was a reasonable value to use in the stochastic simulations. This value of $k_{on\text{-}m}$ is the attachment rate of SxIP to MT lattice, which is constant along the MT and we assumed that was not affected by the tube force. In the absence of EB3, $k_{on\text{-}m}$ had the same value along the MT shaft and at the MT tip, because SxIP molecules at the front of the deformation cannot distinguish between MT shaft and MT tip. The stochastic rate of the attachment transition was $a_{on\text{-}m} = k_{on\text{-}m} * n_m$.

Simulation parameters in the presence of EB3

In the presence of EB3, the formation of a SxIP-EB3 complex imposed a spatial and temporal regulation on $k_{on\text{-}m}$. The association rate of His-GFP-SxIP at MT tips that were not in contact with membranes was 2.5 fold higher than the on-rate of SxIP at the MT shaft (Supplementary Fig. S3e). We assumed that the kinetic constants of SxIP bound to the membrane displayed the same ratio, resulting in $k_{on\text{-}m\text{-}tip} = 2.5 * k_{on\text{-}m}$.

As mentioned above, every elemental stochastic reaction at a given position in the grid depends on the number of available molecules (occupation number). The number of EB3 molecules is high at the plus ends and decays towards the seed along the lattice of the MT, showing a comet-like shape. The distribution of the number of His-GFP-SxIP molecules measured from experiments showed the same pattern (Fig. 1c and Supplementary Fig. S1a). The stochastic rate of the attachment reaction to the tip of SxIP in the presence of EB3 can then be written as $a_{on\text{-}m\text{-}tip}= k_{on\text{-}m\text{-}tip}*n_m*p_{m\text{-}peptide}$, where $p_{m\text{-}peptide}$ is the occupation probability of SxIP along a MT starting from the MT tip measured experimentally (Supplementary Fig. S3j). SxIP molecules that detached from a MT diffused along the membrane with equal probability to the left or to the right. In the discretized representation, the diffusion of the peptides along the deformation is characterized by a constant rate $k_{D\text{-}m}=D_m/d^2$ (ref[27]) with a stochastic rate $a_{D\text{-}m}= k_{D\text{-}m}*n_m$ where D_m is the diffusion coefficient of the peptide on the surface of the GUVs (Supplementary Fig. S3g,h).

Similarly, we considered symmetric diffusion of SxIP molecules bound to a MT, with the stochastic rate $a_{D\text{-}MT}= k_{D\text{-}MT}*n_{MT}$ and $k_{D\text{-}MT}=D_{MT}/d^2$. Here, D_{MT} is the diffusion coefficient of

SxIP molecules bound to the MT we considered that the diffusion rates were not affected by the presence of EB3 or by membrane forces.

Postprocessing of the simulation output

The output of each individual simulation was the position of the membrane tip (sliding along a MT shaft), or the position of the membrane and MT tip. We applied the following rules to sort the deformation events:

1. Events with a deformation of length lower than 200 nm were regarded as non-deformation events with zero length.
2. Evens classified as deformations (length>200 nm) were categorized as short tubes when the tube length was the range of 200-600 nm.
3. Tubes with a length >600 nm were considered as long deformations.
4. Only MTs that grew more than 200 nm were considered for analysis.
5. A detachment event happened when the distance between the membrane tip and the MT tip was longer than 200 nm.

Table 1: Parameters of the model and simulations

Parameter	Description	Value	Source
d	Length of the tubulin dimer	8 nm	Model assumption, see Supplementary note
k_{off}	Dissociation rate of the SxIP from the MT lattice	$1.7 \pm 0.1\ s^{-1}$ (n=217)*	Measured experimentally from single binding events Supplementary Fig. S3c
$k_{off\text{-}m}$	Dissociation rate of the SxIP bound to GUV from the MT lattice	$k_{off\text{-}m} = k_{off}$	Measured experimentally from single binding events Supplementary Fig. S3c
$k_{on\text{-}m} = (\max(V_{spreading})/(d)) + k_{off\text{-}m}$	Association rate of the SxIP with the MT lattice	$16 \pm 8\ s^{-1}$ (n=12)*	Measured experimentally. Supplementary Fig. S3k
$k_{on\text{-}m\text{-}tip}$	Association rate of the SxIP with the MT tip	$40\ s^{-1}$	Based on experimental data see Supplementary note
ξ	Characteristic length of the potential barrier	1 nm	Model assumption, see Supplementary note
n_p	Number of SxIP molecules bound at the tip	1-3	Model assumption, see Supplementary note
σ	Lateral membrane tension	[2e-7,2e-6] N/m	Based on experimental data, Fig. 3h
κ	Bending rigidity of the membrane	[4e-20, 3e-19] J	Based on experimental data, Fig. 3h
R	GUV radius	5-15 μm	Based on experimental data
r_0	Curvature radius of the tether	Calculated as $r_0 = \kappa/(2\sigma)^{1/2}$; ref. 61	Based on experimental data
$p_{m\text{-}peptide}$	Occupation probability of SxIP along a MT starting from the MT tip	Experimentally measured function of distance from microtubule tip	Based on experimental data, see Supplementary note, Supplementary Fig. S3k
$\langle N_{p\text{-}tip} \rangle$	Maximum number of SxIP molecules at the MT tip	28 ± 18 (n=19)**	Based on experimental data
D_{MT}	Diffusion coefficient of SxIP molecules along the MT	$0.03 \pm 0.01 \mu m^2/s$ (n=104)*	Measured experimentally From single binding events Supplementary Fig. S3f
$k_{D\text{-}MT}$	Diffusion rate of SxIP molecules along the MT	$468 \pm 156\ s^{-1}$*	Based on experimental data
D_m	Diffusion coefficient of SxIP molecules bound to the membrane	$4 \pm 2\ \mu m^2/s$ (n=18)**	Measured experimentally by FCS Supplementary Fig. S3h,i
$k_{D\text{-}m}$	Diffusion rate of SxIP molecules bound to the membrane	$56 \pm 31\ ms^{-1}$*	Based on experimental data
w_0	Radius of the laser beam in the focal plane	$0.20 \pm 0.06\ \mu m$ (n=18) **	Measured experimentally by FCS Supplementary Fig. S3g,h
$N_{SxIP\text{-}m}$	Number of SxIP molecules bound to the GUV surface measured at 15 nM of SxIP (measured inside of the focal volume)	5 ± 5 (n=18)**	Measured experimentally Supplementary Fig. S3g,h
$\rho_{SxIP} = N_{SxIP\text{-}m} / w_0$	Surface density of SxIP molecules bound to the GUV surface	125 ± 26 #molecules/μm^2 (n = 18)*	Based on experimental data
$\rho_{SxIP\text{-}MT} = \rho_{SxIP} * (l_{GUV\text{-}MTs\ contact} / l_{GUVS})$	Surface density of SxIP molecules bound to the GUV surface in contact with MTs	250 ± 112 #SxIP/μm^2*	Based on experimental data Fig. 3b

*mean value ± standard error **mean value ± standard deviation

Figure 1

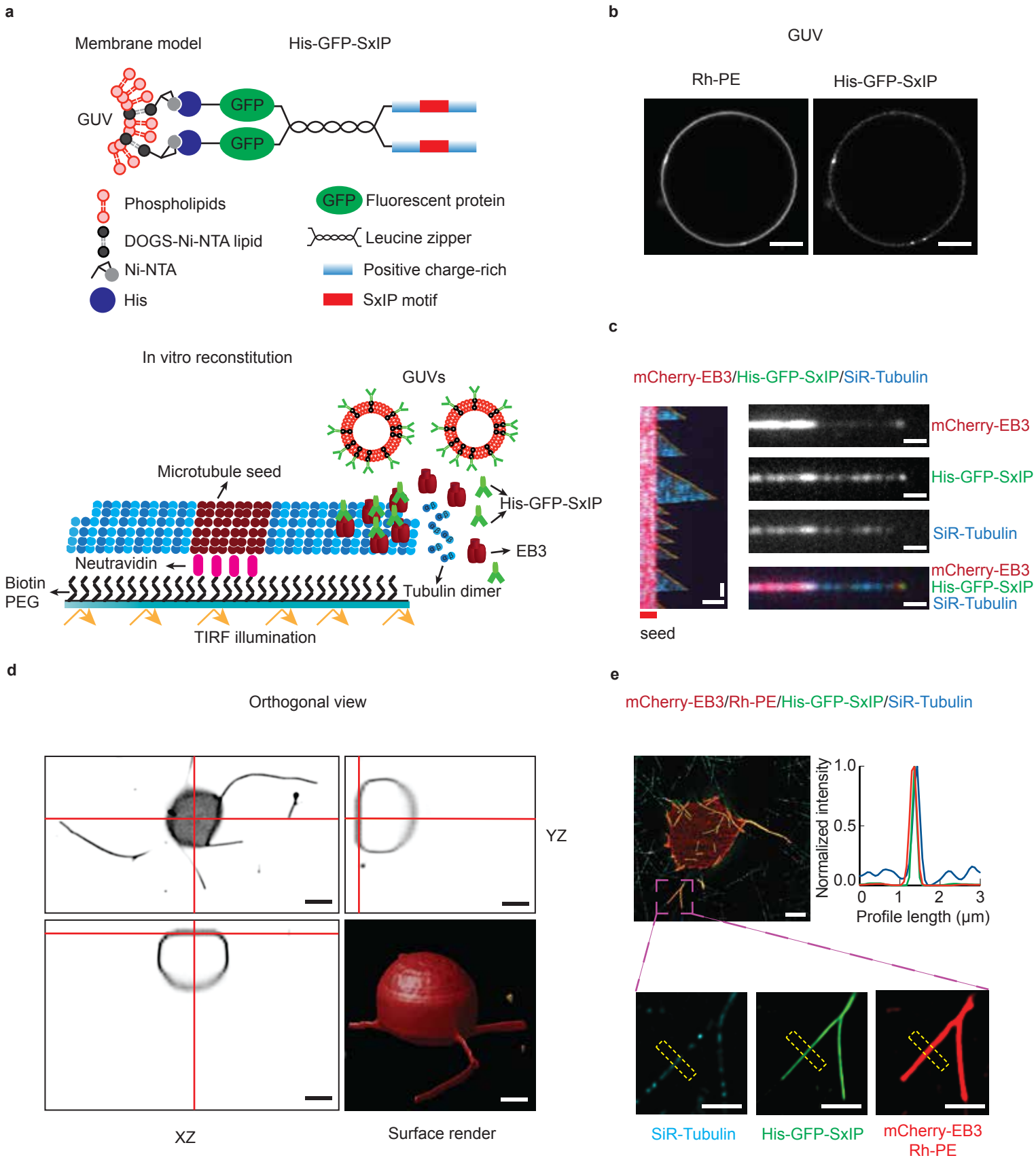
a
Membrane model
His-GFP-SxIP
GUV
GFP
GFP
Phospholipids
DOGS-Ni-NTA lipid
Ni-NTA
His
GFP Fluorescent protein
Leucine zipper
Positive charge-rich
SxIP motif
In vitro reconstitution
GUVs
Microtubule seed
His-GFP-SxIP
EB3
Neutravidin
Biotin
PEG
Tubulin dimer
TIRF illumination
b
GUV
Rh-PE
His-GFP-SxIP
c
mCherry-EB3/His-GFP-SxIP/SiR-Tubulin
mCherry-EB3
His-GFP-SxIP
SiR-Tubulin
mCherry-EB3
His-GFP-SxIP
SiR-Tubulin
seed
d
Orthogonal view
YZ
XZ
Surface render
e
mCherry-EB3/Rh-PE/His-GFP-SxIP/SiR-Tubulin
Normalized intensity
1.0
0.5
0.0
0
1
2
3
Profile length (μm)
SiR-Tubulin
His-GFP-SxIP
mCherry-EB3
Rh-PE

Figure 2

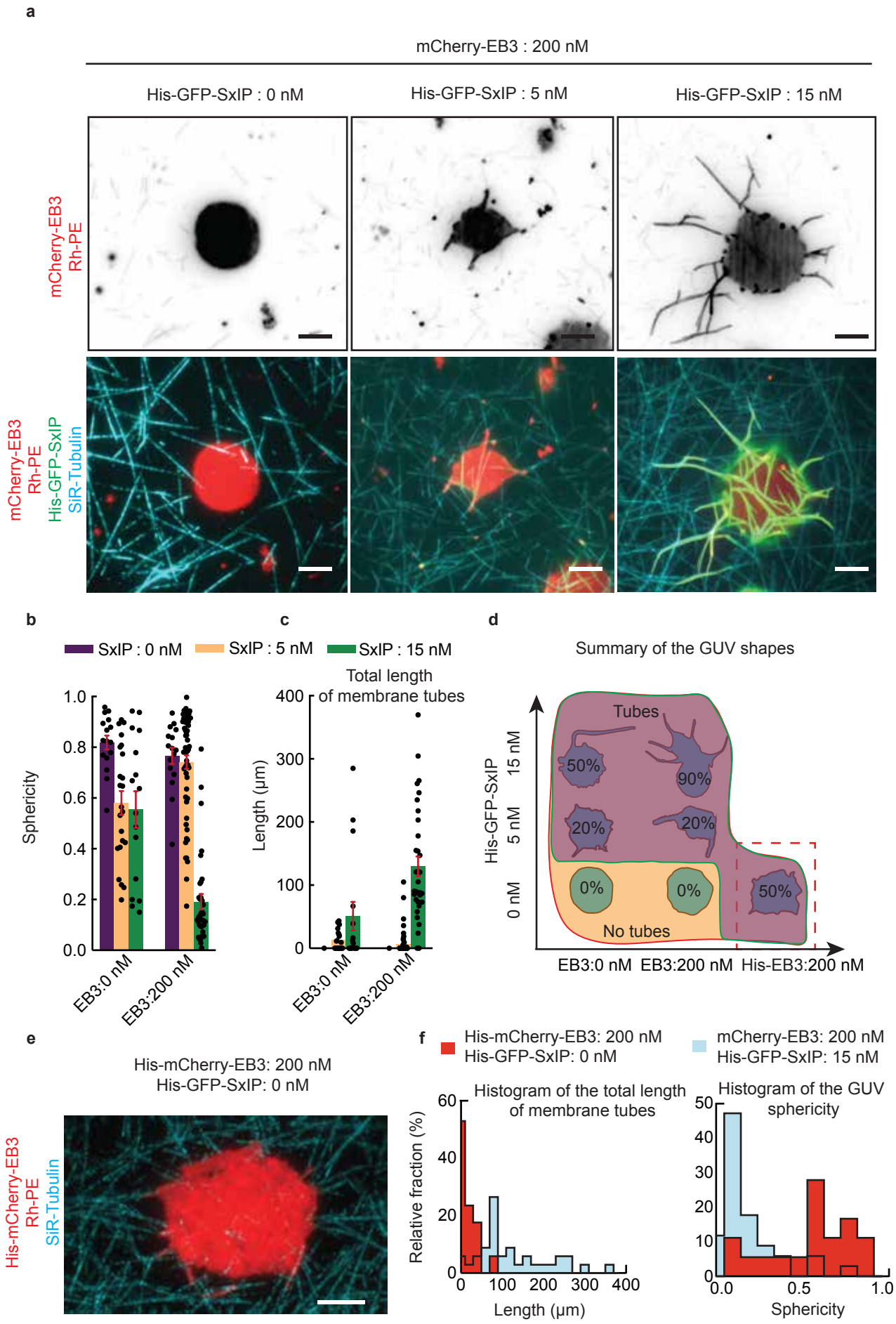
a
mCherry-EB3 : 200 nM
His-GFP-SxIP : 0 nM
His-GFP-SxIP : 5 nM
His-GFP-SxIP : 15 nM
mCherry-EB3
Rh-PE
mCherry-EB3
Rh-PE
His-GFP-SxIP
SiR-Tubulin
b
SxIP : 0 nM
SxIP : 5 nM
SxIP : 15 nM
Sphericity
1.0
0.8
0.6
0.4
0.2
0.0
EB3:0 nM
EB3:200 nM
c
Total length
of membrane tubes
Length (µm)
400
300
200
100
0
EB3:0 nM
EB3:200 nM
d
Summary of the GUV shapes
His-GFP-SxIP
15 nM
5 nM
0 nM
Tubes
50%
90%
20%
20%
0%
0%
50%
No tubes
EB3:0 nM
EB3:200 nM
His-EB3:200 nM
e
His-mCherry-EB3: 200 nM
His-GFP-SxIP: 0 nM
His-mCherry-EB3
Rh-PE
SiR-Tubulin
f
His-mCherry-EB3: 200 nM
His-GFP-SxIP: 0 nM
mCherry-EB3: 200 nM
His-GFP-SxIP: 15 nM
Histogram of the total length
of membrane tubes
Relative fraction (%)
60
40
20
0
0
100
200
300
400
Length (µm)
Histogram of the GUV
sphericity
50
40
30
20
10
0
0.0
0.5
1.0
Sphericity

Figure 3

mCherry-EB3 : 200 nM,His-GFP-SxIP : 15 nM

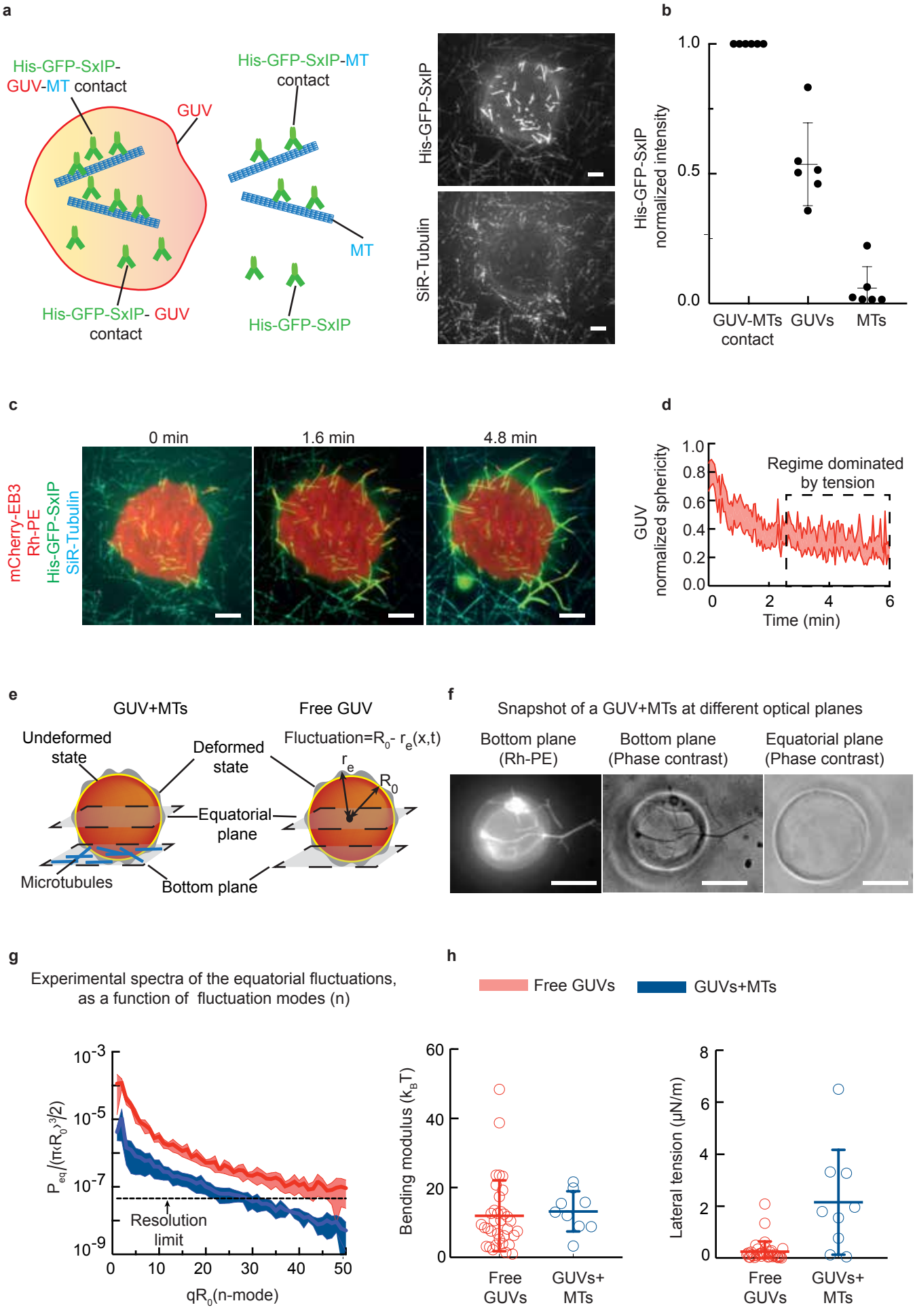

Figure 4

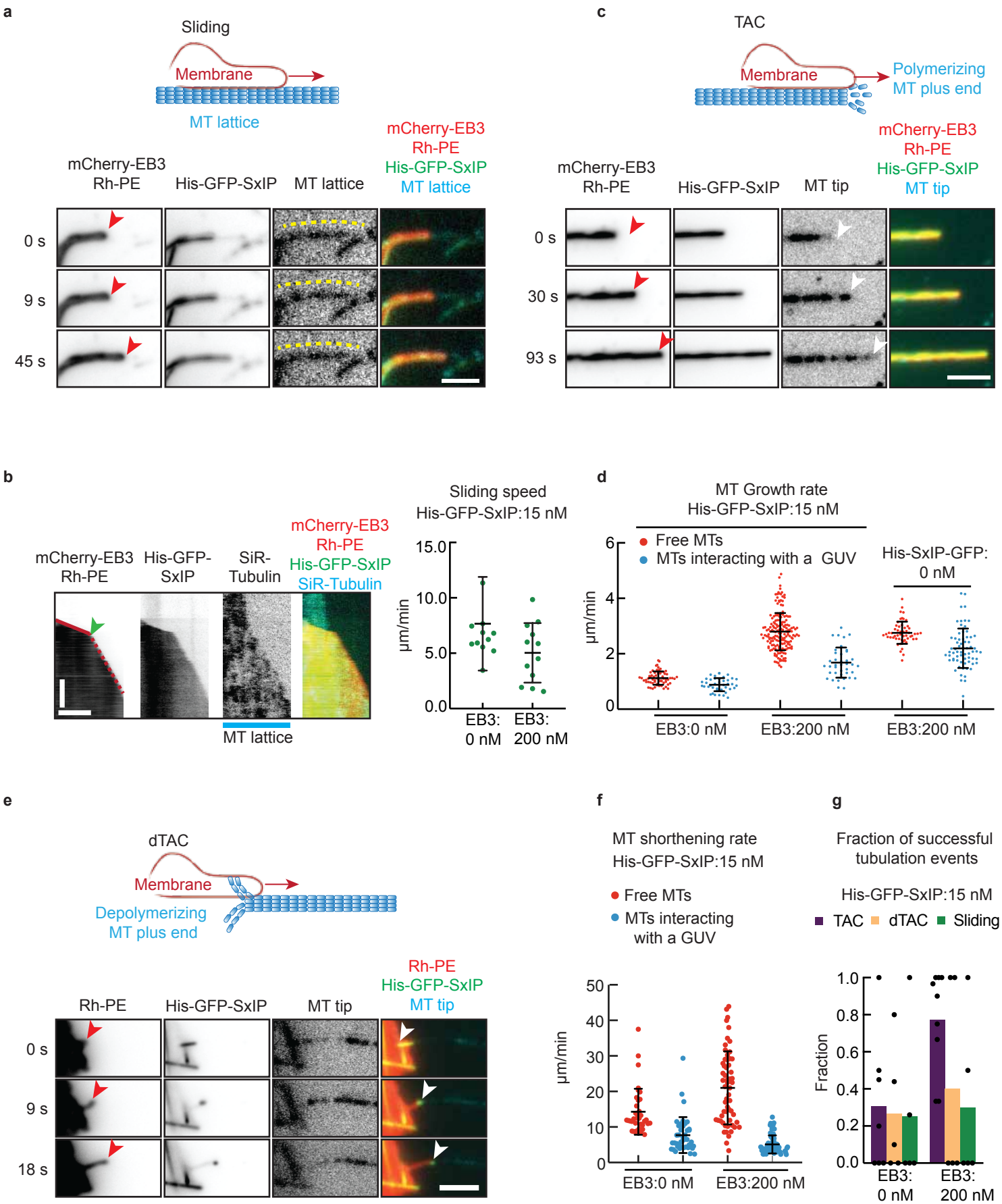
a
Sliding
Membrane
MT lattice
mCherry-EB3
Rh-PE
His-GFP-SxIP
MT lattice
mCherry-EB3
Rh-PE
His-GFP-SxIP
MT lattice
0 s
9 s
45 s
c
TAC
Membrane
Polymerizing
MT plus end
mCherry-EB3
Rh-PE
His-GFP-SxIP
MT tip
mCherry-EB3
Rh-PE
His-GFP-SxIP
MT tip
0 s
30 s
93 s
b
mCherry-EB3
Rh-PE
His-GFP-
SxIP
SiR-
Tubulin
mCherry-EB3
Rh-PE
His-GFP-SxIP
SiR-Tubulin
MT lattice
Sliding speed
His-GFP-SxIP:15 nM
µm/min
15.0
10.0
5.0
0.0
EB3:
0 nM
EB3:
200 nM
d
MT Growth rate
His-GFP-SxIP:15 nM
Free MTs
MTs interacting with a GUV
His-SxIP-GFP:
0 nM
µm/min
6
4
2
0
EB3:0 nM
EB3:200 nM
EB3:200 nM
e
dTAC
Membrane
Depolymerizing
MT plus end
Rh-PE
His-GFP-SxIP
MT tip
Rh-PE
His-GFP-SxIP
MT tip
0 s
9 s
18 s
f
MT shortening rate
His-GFP-SxIP:15 nM
Free MTs
MTs interacting
with a GUV
µm/min
50
40
30
20
10
0
EB3:0 nM
EB3:200 nM
g
Fraction of successful
tubulation events
His-GFP-SxIP:15 nM
TAC
dTAC
Sliding
Fraction
1.0
0.8
0.6
0.4
0.2
0.0
EB3:
0 nM
EB3:
200 nM

Figure 5

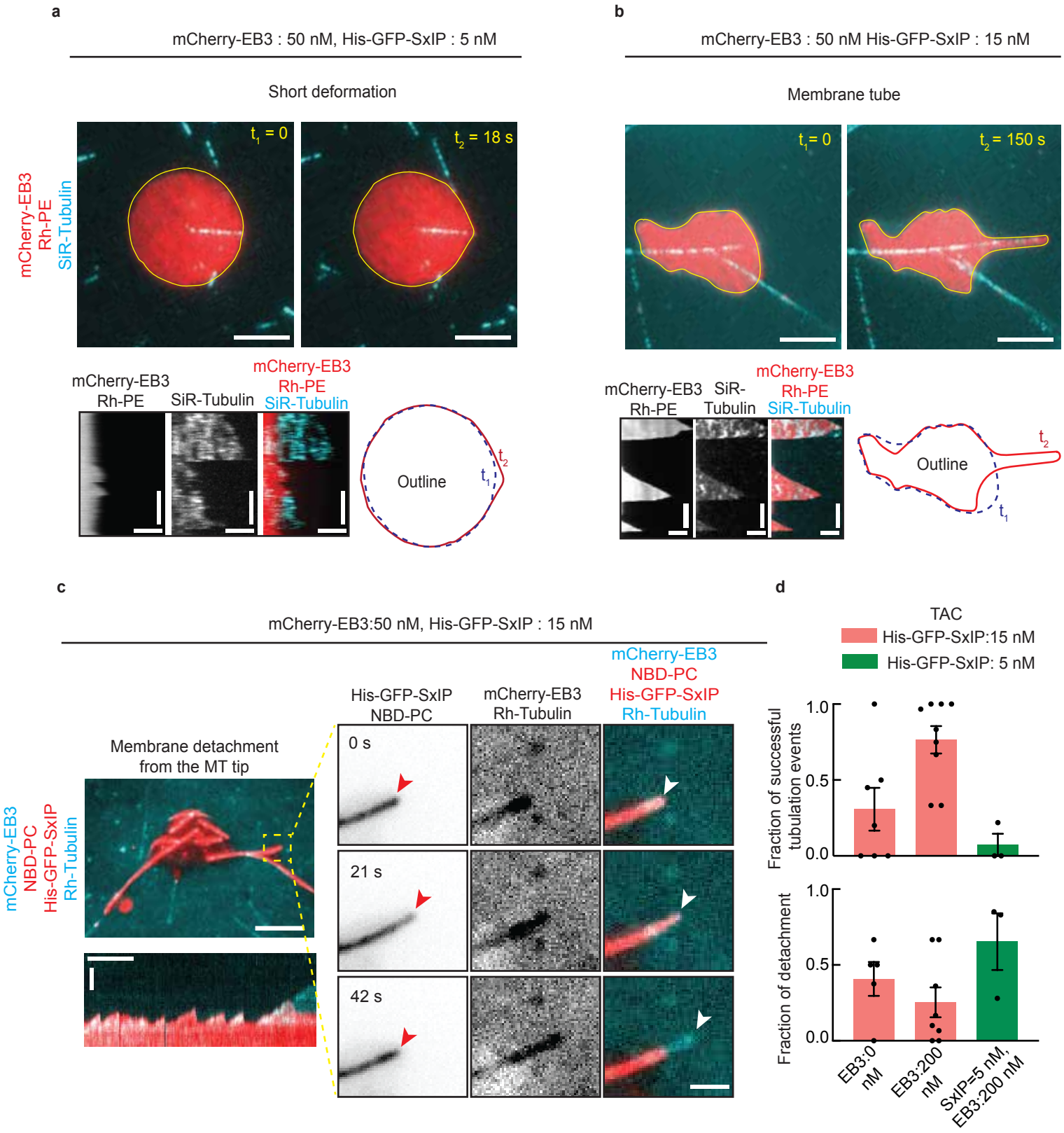
a
mCherry-EB3 : 50 nM, His-GFP-SxIP : 5 nM
Short deformation
mCherry-EB3
Rh-PE
SiR-Tubulin
t1 = 0
t2 = 18 s
mCherry-EB3
Rh-PE
SiR-Tubulin
mCherry-EB3
Rh-PE
SiR-Tubulin
Outline
t1
t2
b
mCherry-EB3 : 50 nM His-GFP-SxIP : 15 nM
Membrane tube
t1= 0
t2 = 150 s
mCherry-EB3
Rh-PE
SiR-Tubulin
mCherry-EB3
Rh-PE
SiR-Tubulin
Outline
t2
t1
c
mCherry-EB3:50 nM, His-GFP-SxIP : 15 nM
Membrane detachment
from the MT tip
mCherry-EB3
NBD-PC
His-GFP-SxIP
Rh-Tubulin
His-GFP-SxIP
NBD-PC
mCherry-EB3
Rh-Tubulin
mCherry-EB3
NBD-PC
His-GFP-SxIP
Rh-Tubulin
0 s
21 s
42 s
d
TAC
His-GFP-SxIP:15 nM
His-GFP-SxIP: 5 nM
Fraction of successful
tubulation events
1.0
0.5
0.0
Fraction of detachment
1.0
0.5
0.0
EB3:0
nM
EB3:200
nM
SxIP=5 nM,
EB3:200 nM

Figure 6

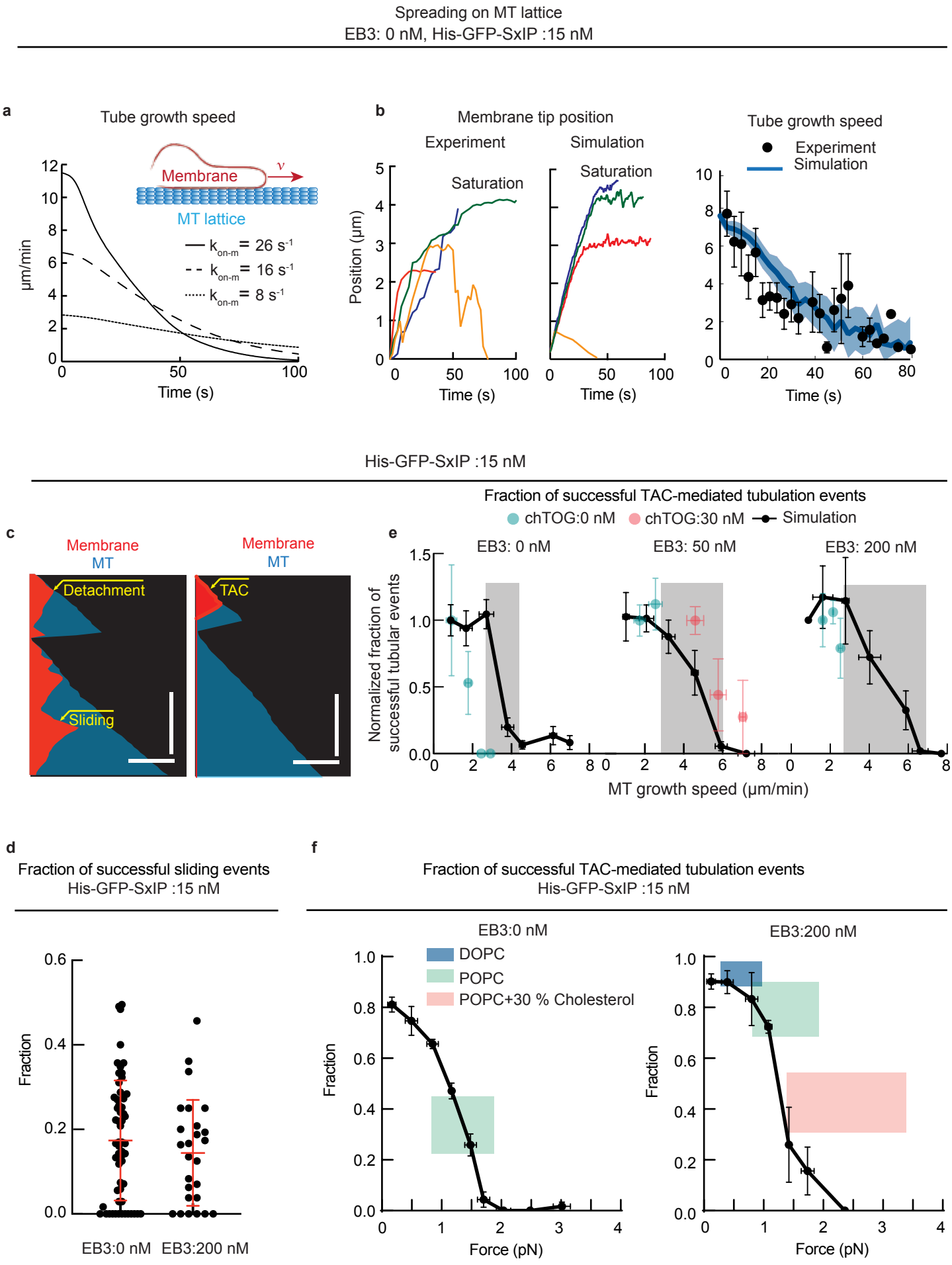
Spreading on MT lattice
EB3: 0 nM, His-GFP-SxIP :15 nM
a
Tube growth speed
Membrane
MT lattice
k_{on-m} = 26 s^{-1}
k_{on-m} = 16 s^{-1}
k_{on-m} = 8 s^{-1}
µm/min
Time (s)
b
Membrane tip position
Experiment
Simulation
Saturation
Position (µm)
Time (s)
Tube growth speed
Experiment
Simulation
His-GFP-SxIP :15 nM
c
Membrane
MT
Detachment
Sliding
TAC
Fraction of successful TAC-mediated tubulation events
chTOG:0 nM
chTOG:30 nM
Simulation
e
EB3: 0 nM
EB3: 50 nM
EB3: 200 nM
Normalized fraction of successful tubular events
MT growth speed (µm/min)
d
Fraction of successful sliding events
His-GFP-SxIP :15 nM
Fraction
EB3:0 nM
EB3:200 nM
f
Fraction of successful TAC-mediated tubulation events
His-GFP-SxIP :15 nM
EB3:0 nM
EB3:200 nM
DOPC
POPC
POPC+30 % Cholesterol
Fraction
Force (pN)

Figure 7

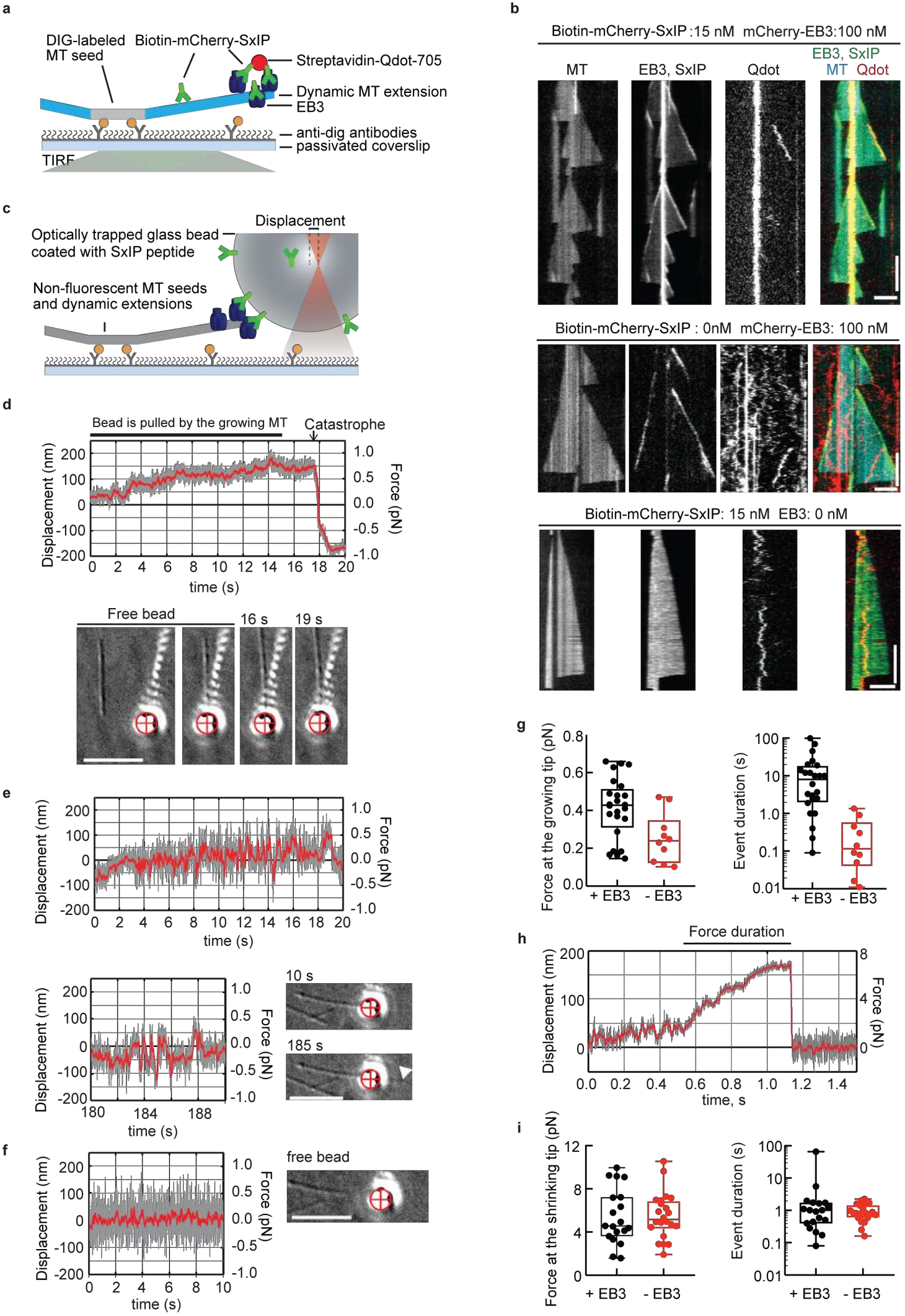
a
DIG-labeled MT seed
Biotin-mCherry-SxIP
Streptavidin-Qdot-705
Dynamic MT extension
EB3
anti-dig antibodies
passivated coverslip
TIRF
b
Biotin-mCherry-SxIP :15 nM mCherry-EB3:100 nM
MT
EB3, SxIP
Qdot
EB3, SxIP
MT Qdot
Biotin-mCherry-SxIP : 0nM mCherry-EB3: 100 nM
Biotin-mCherry-SxIP: 15 nM EB3: 0 nM
c
Displacement
Optically trapped glass bead coated with SxIP peptide
Non-fluorescent MT seeds and dynamic extensions
d
Bead is pulled by the growing MT
Catastrophe
Displacement (nm)
Force (pN)
time (s)
Free bead
16 s
19 s
e
Displacement (nm)
Force (pN)
time (s)
10 s
185 s
f
free bead
Displacement (nm)
Force (pN)
time (s)
g
Force at the growing tip (pN)
Event duration (s)
+ EB3
- EB3
h
Force duration
Displacement (nm)
Force (pN)
time, s
i
Force at the shrinking tip (pN)
Event duration (s)
+ EB3
- EB3

Figure S1

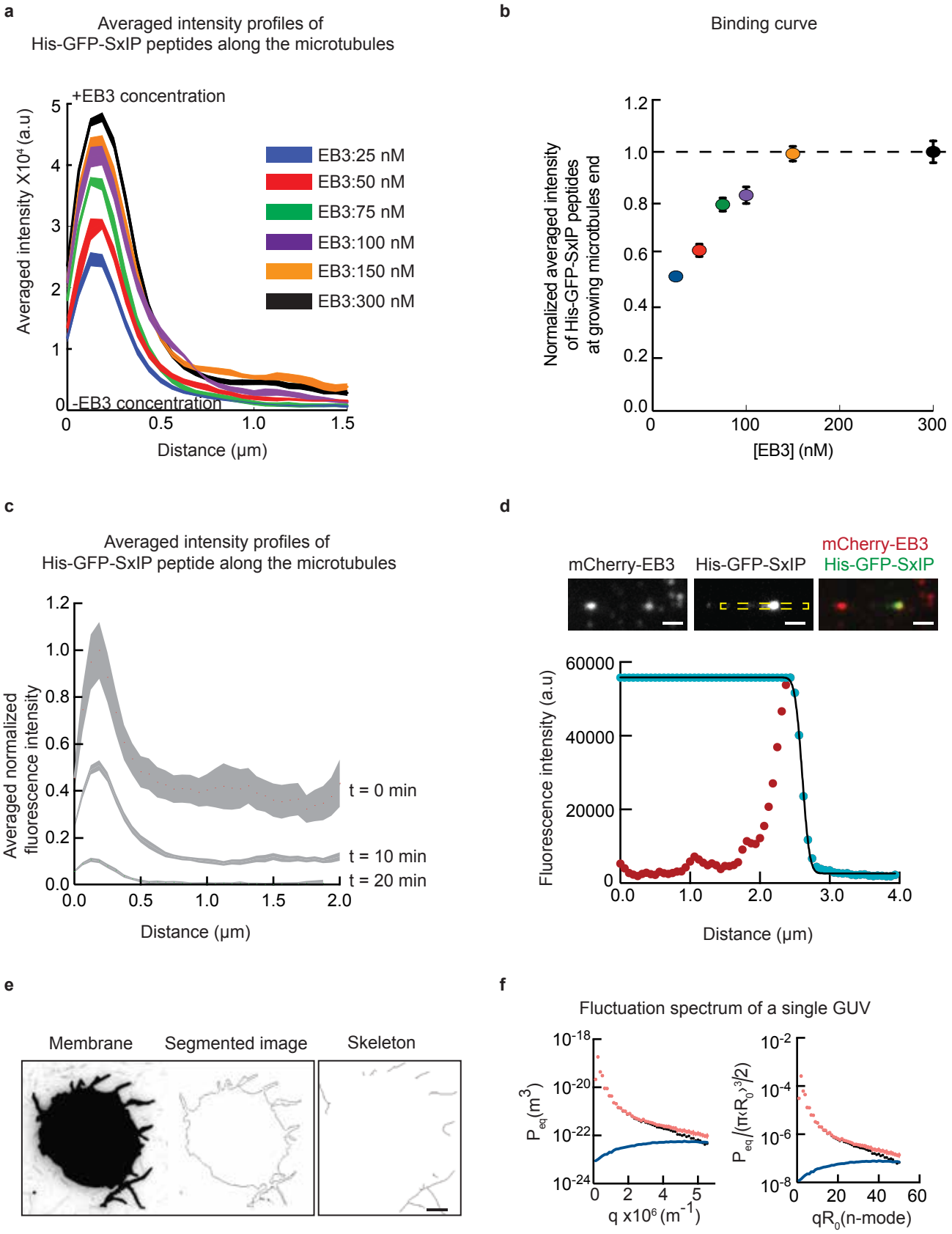

a
Averaged intensity profiles of
His-GFP-SxIP peptides along the microtubules
+EB3 concentration
-EB3 concentration
Averaged intensity X10⁴ (a.u)
Distance (μm)
EB3:25 nM
EB3:50 nM
EB3:75 nM
EB3:100 nM
EB3:150 nM
EB3:300 nM
b
Binding curve
Normalized averaged intensity
of His-GFP-SxIP peptides
at growing microtbules end
[EB3] (nM)
c
Averaged intensity profiles of
His-GFP-SxIP peptide along the microtubules
Averaged normalized
fluorescence intensity
Distance (μm)
t = 0 min
t = 10 min
t = 20 min
d
mCherry-EB3
His-GFP-SxIP
mCherry-EB3
His-GFP-SxIP
Fluorescence intensity (a.u)
Distance (μm)
e
Membrane
Segmented image
Skeleton
f
Fluctuation spectrum of a single GUV
P_eq(m³)
q x10⁶ (m⁻¹)
P_eq/(π‹R₀›³/2)
qR₀(n-mode)

Figure S2

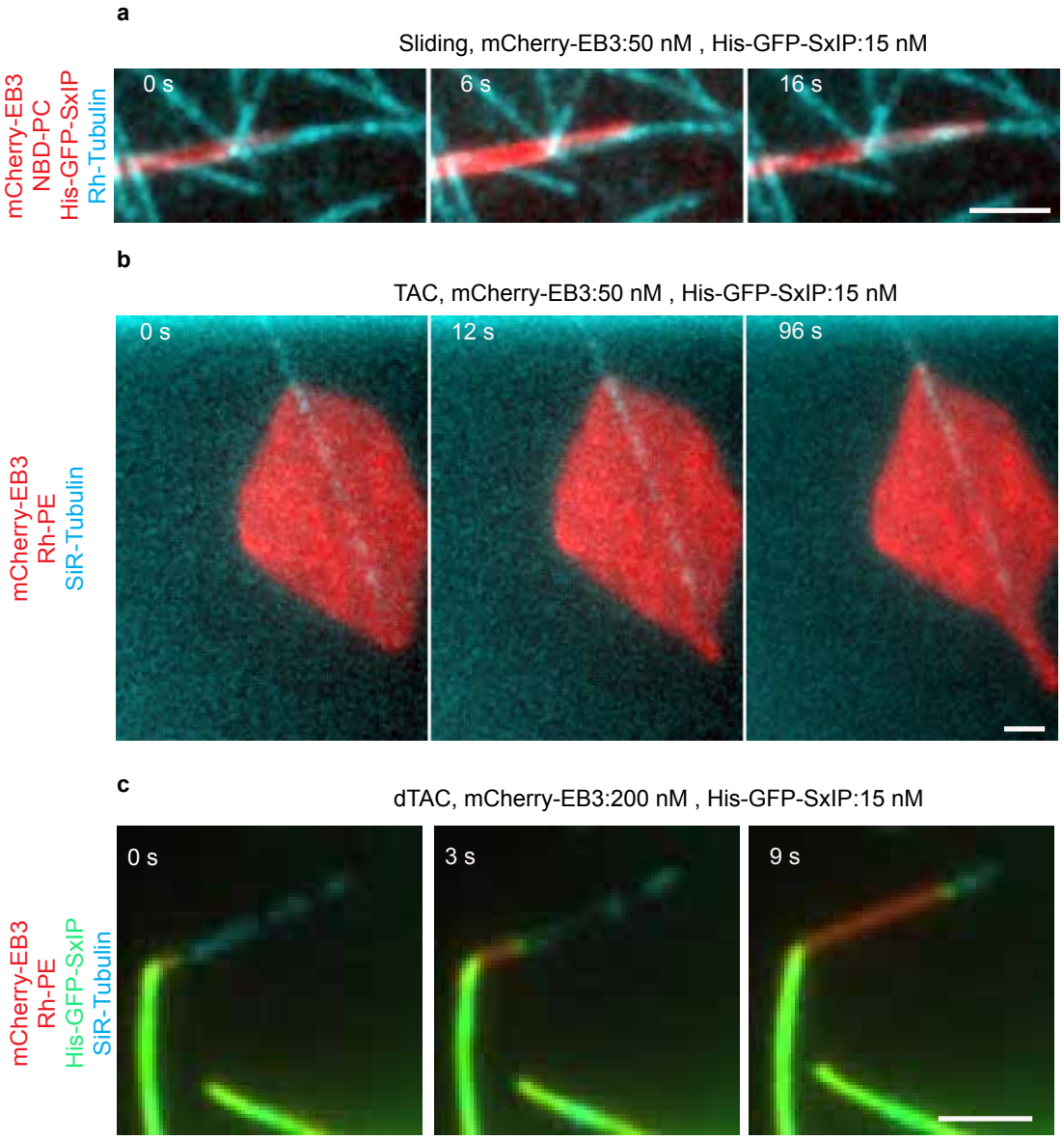
a
Sliding, mCherry-EB3:50 nM , His-GFP-SxIP:15 nM
mCherry-EB3
NBD-PC
His-GFP-SxIP
Rh-Tubulin
0 s
6 s
16 s
b
TAC, mCherry-EB3:50 nM , His-GFP-SxIP:15 nM
mCherry-EB3
Rh-PE
SiR-Tubulin
0 s
12 s
96 s
c
dTAC, mCherry-EB3:200 nM , His-GFP-SxIP:15 nM
mCherry-EB3
Rh-PE
His-GFP-SxIP
SiR-Tubulin
0 s
3 s
9 s

Figure S3

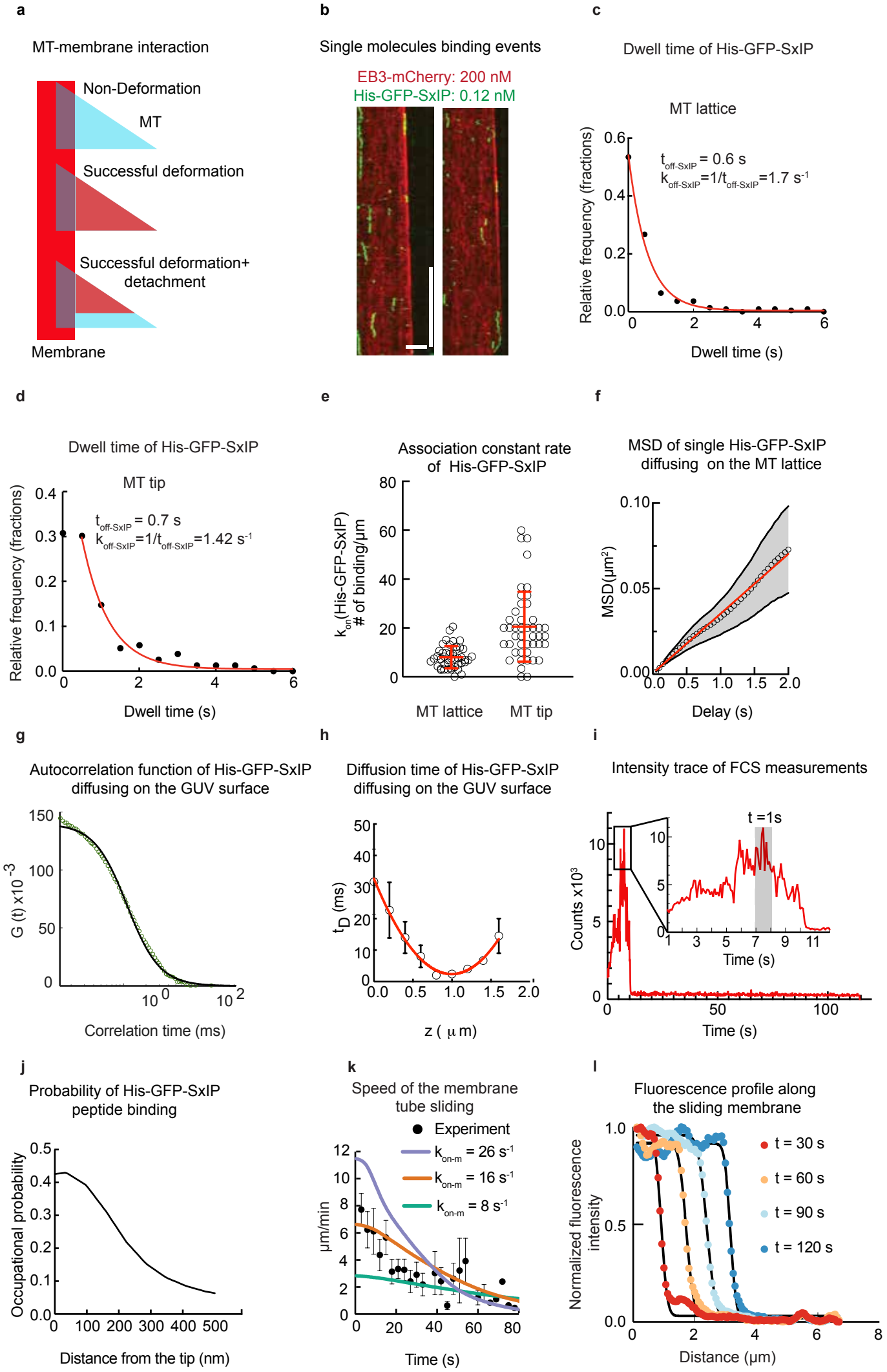
a
MT-membrane interaction
Non-Deformation
MT
Successful deformation
Successful deformation+ detachment
Membrane
b
Single molecules binding events
EB3-mCherry: 200 nM
His-GFP-SxIP: 0.12 nM
c
Dwell time of His-GFP-SxIP
MT lattice
$t_{off\text{-}SxIP}$ = 0.6 s
$k_{off\text{-}SxIP}=1/t_{off\text{-}SxIP}$=1.7 s^{-1}
Relative frequency (fractions)
Dwell time (s)
d
Dwell time of His-GFP-SxIP
MT tip
$t_{off\text{-}SxIP}$ = 0.7 s
$k_{off\text{-}SxIP}=1/t_{off\text{-}SxIP}$=1.42 s^{-1}
Relative frequency (fractions)
Dwell time (s)
e
Association constant rate of His-GFP-SxIP
k_{on}(His-GFP-SxIP) # of binding/µm
MT lattice
MT tip
f
MSD of single His-GFP-SxIP diffusing on the MT lattice
MSD(µm²)
Delay (s)
g
Autocorrelation function of His-GFP-SxIP diffusing on the GUV surface
G (t) x10 -3
Correlation time (ms)
h
Diffusion time of His-GFP-SxIP diffusing on the GUV surface
t_D (ms)
z (µm)
i
Intensity trace of FCS measurements
t =1s
Counts x10³
Time (s)
j
Probability of His-GFP-SxIP peptide binding
Occupational probability
Distance from the tip (nm)
k
Speed of the membrane tube sliding
Experiment
$k_{on\text{-}m}$ = 26 s^{-1}
$k_{on\text{-}m}$ = 16 s^{-1}
$k_{on\text{-}m}$ = 8 s^{-1}
µm/min
Time (s)
l
Fluorescence profile along the sliding membrane
t = 30 s
t = 60 s
t = 90 s
t = 120 s
Normalized fluorescence intensity
Distance (µm)

Figure S4

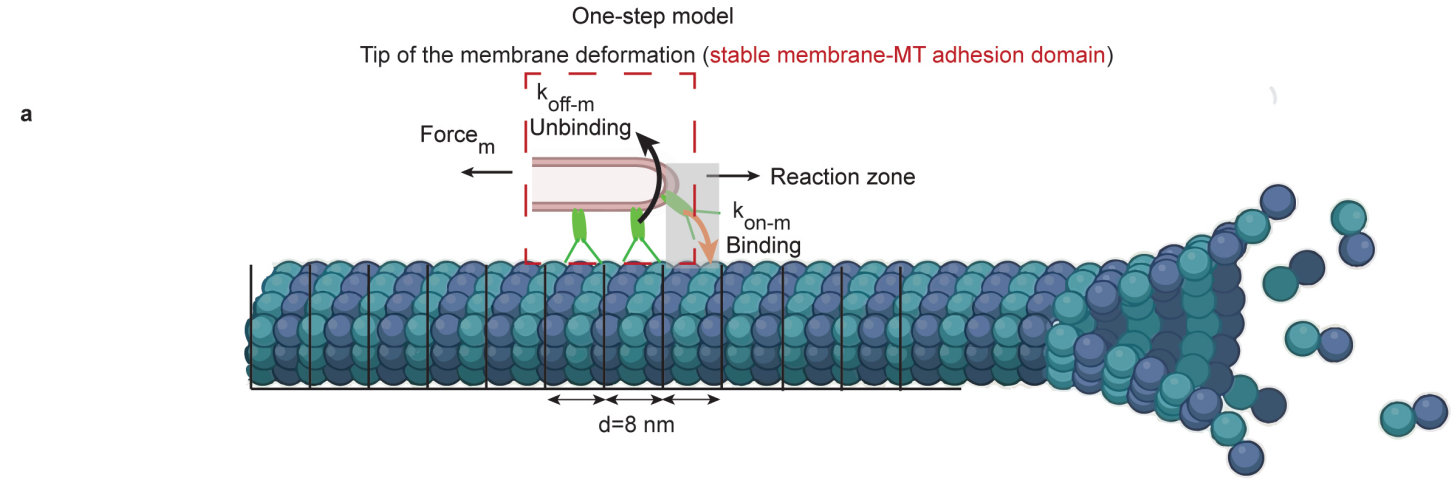
a
One-step model
Tip of the membrane deformation (stable membrane-MT adhesion domain)
k_{off-m}
Unbinding
$Force_m$
Reaction zone
k_{on-m}
Binding
d=8 nm

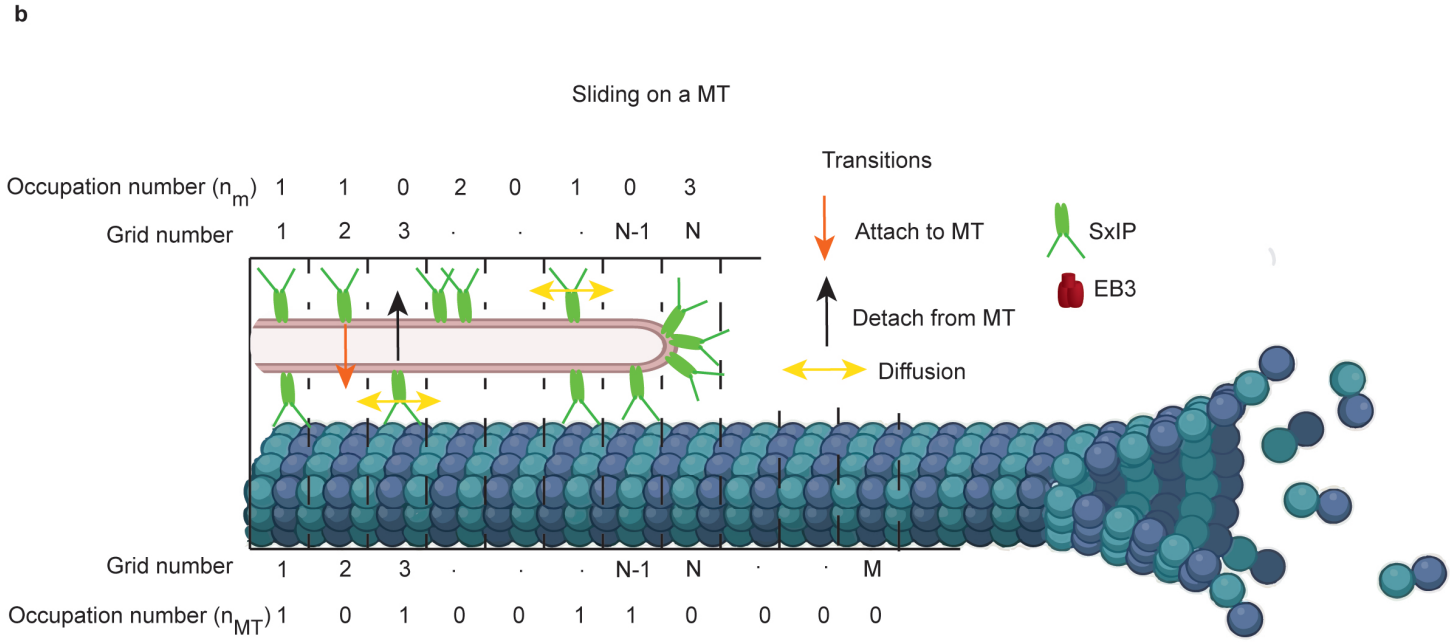
b
Sliding on a MT
Transitions
Occupation number (n_m) 1 1 0 2 0 1 0 3
Grid number 1 2 3 . . . N-1 N
Attach to MT
SxIP
EB3
Detach from MT
Diffusion
Grid number 1 2 3 . . . N-1 N . . M
Occupation number (n_{MT}) 1 0 1 0 0 1 1 0 0 0 0

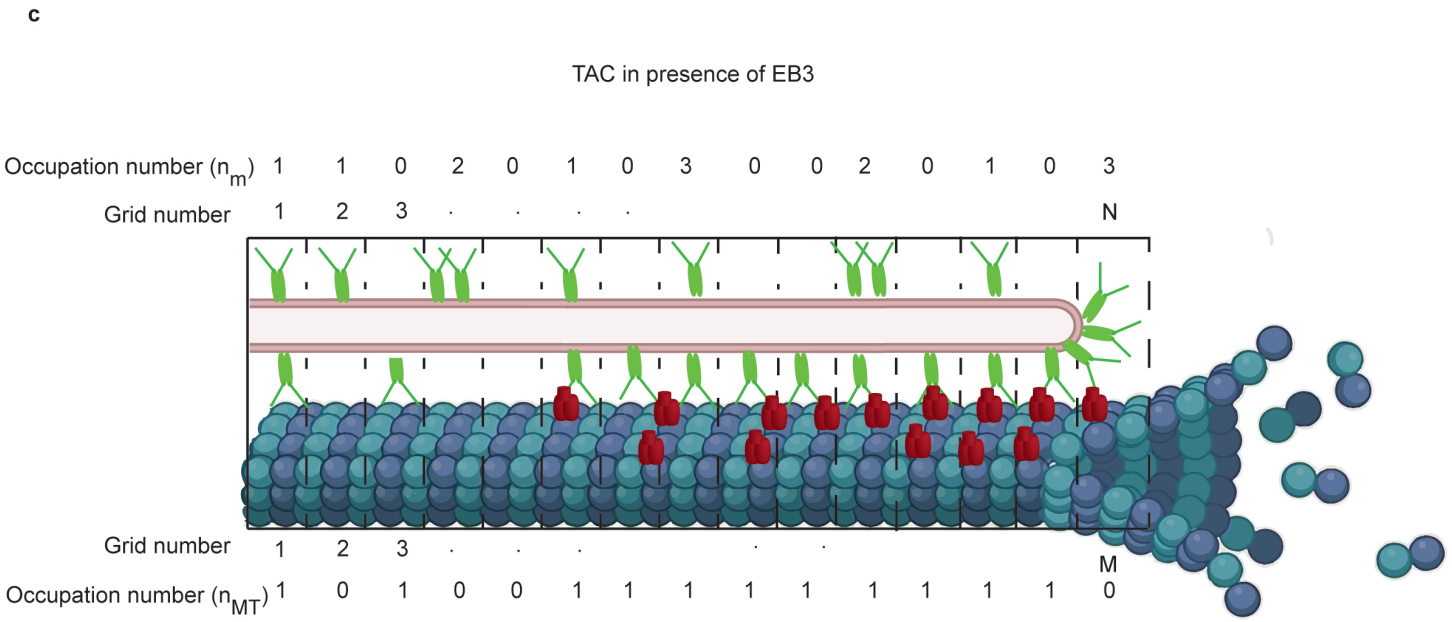
c
TAC in presence of EB3
Occupation number (n_m) 1 1 0 2 0 1 0 3 0 0 2 0 1 0 3
Grid number 1 2 3 . . . . N
Grid number 1 2 3 . . . . . M
Occupation number (n_{MT}) 1 0 1 0 0 1 1 1 1 1 1 1 1 1 0